Materials

SOLIDIFICATION

J. A. Dantzig and M. Rappaz

EPFL Press
Distributed by CRC Press

SOLIDIFICATION

Engineering Sciences *Materials*

SOLIDIFICATION

J. A. Dantzig and M. Rappaz

A full list of errata, related software packages,
a complete set of figures for teaching purposes,
and other materials are available at:
www.solidification.org

EPFL Press
A Swiss academic publisher distributed by CRC Press

CRC Press
Taylor & Francis Group

Taylor and Francis Group, LLC
6000 Broken Sound Parkway, NW, Suite 300,
Boca Raton, FL 33487

Distribution and Customer Service
orders@crcpress.com

www.crcpress.com

Library of Congress Cataloging-in-Publication Data
A catalog record for this book is available from the Library of Congress.

The authors and publisher express their thanks to the Ecole polytechnique fédérale de Lausanne (EPFL) for its generous support towards the publication of this book.

The series *Materials* is published under the editorial direction of
Professor Michel Rappaz (EPFL).

Previous volumes:
Corrosion and Surface Chemistry of Metals
Dieter Landolt

Cover design by Sébastien Rappaz

EPFL Press

is an imprint owned by Presses polytechniques et universitaires romandes, a Swiss academic publishing company whose main purpose is to publish the teaching and research works of the Ecole polytechnique fédérale de Lausanne.

Presses polytechniques et universitaires romandes, EPFL – Olibu Ib^okfkd @bkqbo,
Post office box 119, CH-1015 Lausanne, Switzerland
E-Mail: ppur@epfl.ch, Phone: 021/693 21 30, Fax: 021/693 40 27

www.epflpress.org * t t t+p1ifafcf`^qf1k+1od

© 2009, First edition, EPFL Press
ISBN 978-2-940222-17-9 (EPFL Press)
ISBN 978-0-8493-8238-3 (CRC Press)

Fkaf^k bafqf1k) mrinted in Fkaf^

PREFACE

The modern science of solidification began in the 1940's, when engineers began to use analytical methods and models to describe solidification processes. In 1940, Chvorinov applied the analysis of heat flow to predict solidification patterns and defects in sand castings. In the 1950's Chalmers and co-workers analyzed the heat and solute balance at the moving solid-liquid interface to understand why planar interfaces become unstable during unidirectional growth. This body of work culminated in a seminal text, *Principles of Solidification*, written by Chalmers in 1964.

In the 1960's, Mullins and Sekerka put Chalmers' analysis on a firmer mathematical footing by performing a formal stability analysis. Later in the 1960's and in the 1970's, Flemings and co-workers developed models for segregation and other microstructural features by applying heat and solute balances at the scale of the microstructural features themselves. Flemings followed Chalmers' text with *Solidification Processing* in 1974, presenting this next generation of achievements.

The next decade saw a great deal of activity in the study of microstructure as a pattern selection problem through the competition between the transport of heat and solute and inherent length scales in the material owing to surface energy. This body of work was summarized in 1984 in *Fundamentals of Solidification*, by Kurz and Fisher.

Kurz and Fisher's book appeared just at the beginning of a revolution in modeling of solidification, when low-cost powerful computers became available. Computational approaches allowed more accurate and detailed models to be constructed, shedding light on many important phenomena. Today, industrial users regularly model the solidification of geometrically complex parts ranging from directionally solidified turbine blades to automotive engines. At the microscopic scale, computational models have been used to great effect to understand the pattern selection process in ways that were only hinted at using the analytical techniques available earlier. In the 1990's, methods were developed to combine these microscopic and macroscopic views of solidification processes.

Although there have been a few specialty texts written in the intervening time between Kurz and Fisher's book and the present, none of them provides a comprehensive presentation of the fundamentals, analytical models, and computational approaches. Also in the 1990's and 2000's, a short course on solidification was developed in collaboration with

Ecole des Mines de Nancy, EPFL and Calcom, that incorporated both the fundamental aspects described earlier and the developing computational techniques. Through teaching this course, and at our respective universities, we felt that there was a need for a new text, which led us to write the book you now hold in your hands. The subject is presented in three parts: *Fundamentals*, which provides the basics of thermodynamics, phase diagrams, and modeling techniques. *Microstructure* then uses these techniques to describe the evolution of the solid at the microscopic scale, from nucleation to dendrites, eutectics and peritectics to microsegregation. This section concludes with a chapter on coupling macro- and micro-models of solidification. The final part, *Defects*, uses the same principles to describe porosity, hot tearing and macrosegregation. We have striven to present this wide range of topics in a comprehensive way, and in particular to use consistent notation throughout.

Acknowledgment

This work represents the culmination of our education, training and practice over the last 25 years. We have had many mentors, colleagues and friends who have helped us along the way, too numerous to name them all. We would particularly like to express our gratitude to our mentors, Wilfried Kurz, Stephen Davis and Robert Pond, Sr. In addition to the authors mentioned above, we would like to acknowledge the very fruitful discussions we have had over the years with many esteemed colleagues: William Boettinger, Martin Glicksman, John Hunt, Alain Karma and Rohit Trivedi, to name just a few. Much of the structure of this text derived from the short course described above, and we would like to thank our colleagues and fellow teachers in that course, past and present, in particular Philippe Thévoz and Marco Gremaud who organize the course. Special thanks are due to Christoph Beckermann, Hervé Combeau, Arne Dahle and Mathis Plapp for their helpful comments and contributions to the manuscript, and to Sébastien Rappaz for the design of the cover. We also owe a special debt of gratitude to our students, postdocs and coworkers, whose contributions made this book possible. We would also like to thank our many colleagues and friends who graciously allowed us to use figures and movie sequences that appear throughout the book.

Most importantly, we would like to thank our families for their love and support.

Jonathan A. Dantzig
Michel Rappaz
Lausanne, 2009

CONTENTS

NOMENCLATURE AND DIMENSIONLESS GROUPS

Principal Nomenclature

A book that covers as many topics as this one does is bound to encounter some problems with nomenclature. We have tried to use standard notation wherever possible, and to be consistent in usage throughout. In order to help distinguish between dimensional quantities and their dimensionless counterparts after scaling, we use Roman alphabet symbols for dimensional variables and corresponding Greek letters for the dimensionless ones. For example, the dimensional coordinates $(x, y, z) \rightarrow (\xi, \eta, \zeta)$. For some variables, such as velocity $\boldsymbol{v}, v_i$, this scheme is not possible because there is no Greek counterpart. Further, we need symbols for both the vector and its components. We handle this by using italic symbols for dimensional quantities and Roman symbols for the dimensionless ones, e.g., $(\boldsymbol{v}, v_i) \rightarrow (\mathbf{v}, \mathrm{v}_i)$.

Subscripts and superscripts can be complicated as well. We use upper case Roman letters to designate components, lower case Greek to represent phases, s or ℓ to designate solid and liquid, respectively, and a superscript '$*$' to designate quantities evaluated at the solid-liquid interface. Whereas the '$*$' will always appear as a superscript, the other indices may appear as subscripts or superscripts, depending on what form provides the clearest description in the current context. As an example, the most complicated symbol used in the text is $C_{J\ell}^{*\alpha}$, which means the mass fraction of component J in the liquid, evaluated at the solid-liquid interface ahead of phase α. This symbol appears in the discussion of the solidification of eutectic and peritectic alloys. The most important symbols are given below.

Roman alphabet

$\mathrm{A}, \mathrm{B}, \ldots$	species (component) A
A, $A_{s\ell}$	area, solid-liquid interfacial area
$A_{f\ell}$, A_{fs}	surface area between foreign substrate and liquid, or foreign substrate and solid
A_C, A_R	growth constants for eutectics
$A(\boldsymbol{n})$	surface energy anisotropy function

$a_1, a_2, a_3, \ldots$	surface energy anisotropy coefficients
$a_{A\alpha}$	chemical activity of species A in phase α
B	ratio of solutal and thermal expansion coefficients ($= \beta_C/(m_\ell \beta_T)$)
$[\boldsymbol{B}^e]$	spatial derivatives of element shape functions
$\boldsymbol{b}$	vector of body force per unit mass; design vector
$[\boldsymbol{C}^e], [\boldsymbol{C}]$	element and global capacitance matrices in FEM
C	mass fraction of solute in a binary alloy
C_J	mass fraction of species J in a mixture
C_s^*, C_ℓ^*	mass fractions of solute in the solid and liquid phases of a binary alloy at the solid-liquid interface
c_0, c_1, $\ldots$	constants of integration
c_p, c_V	specific heat at constant pressure; at constant volume
D	chemical diffusivity of solute; diameter
d	diameter of a sphere
$\boldsymbol{D}$	rate-of-deformation tensor ($= (\nabla \boldsymbol{v} + (\nabla \boldsymbol{v})^T)/2$)
d_0, d_0^C	thermal capillary length; chemical capillary length
E	Young's modulus
E, E^m, e	total, molar and specific internal energy
$\dot{E}$	cumulative average deformation rate
$\boldsymbol{\mathcal{E}}$, $\mathcal{E}_{ijkl}$	elasticity tensor, indecial form
e_J^I	second-order interaction coefficient between solute element I and gas element J
$\mathcal{F}, F$	total and volumetric free energy in phase-field model
$\boldsymbol{F}$	deformation gradient tensor, $F_{ij} = \partial x_i/\partial X_j$
f_A, f_V	geometric factors for nucleation in a conical pit
$f_{J\ell}, f_{J\ell}^0$	activity coefficient for species J in an alloy and in a pure material
f_α	mass fraction of phase α
G	temperature gradient
G, G^m, g	total, molar and specific Gibbs free energy
G_C	composition gradient
g	acceleration due to gravity, 9.82 m s^{-2}
g_α	volume fraction of phase α
g_d, g_e, g_g	volume fraction of interdendritic liquid, extradendritic liquid and grain
g_s	volume fraction of solid
g_{se}	extended volume fraction of the solid phase
g_{si}	internal volume fraction of the solid phase in a grain
H, H^m, h	total, molar and specific enthalpy
h_T	heat transfer coefficient
$\boldsymbol{I}$	unit tensor (identity tensor); the ij component is δ_{ij}
I^{homo}, I^{heter}	homogeneous or heterogeneous nucleation rate
I_0^{homo}, I_0^{heter}	prefactors for homogeneous or heterogeneous nucleation rate
Iv_{2D}, Iv_{3D}	Ivantsov function in 2-D or 3-D
i	$\sqrt{-1}$
$\boldsymbol{j}_A$	mass fraction flux for species A
J	Jacobian ($\det \boldsymbol{F}$)
$[\boldsymbol{J}]$	element Jacobian for isoparametric FEM

$\boldsymbol{K}, K$	permeability tensor; value of isotropic permeability
$[\boldsymbol{K}^e], [\boldsymbol{K}]$	element and global conductance matrices in FEM
$\boldsymbol{k}, k$	thermal conductivity tensor; value of isotropic conductivity
k_T	thermal conductivity ratio ($= k_s/k_\ell$)
k_0, k_0^m	partition coefficient (mass); partition coefficient (molar)
k_B	Boltzmann's constant, 1.38×10^{-23} J K^{-1}
L, L_c	characteristic length
L_f	latent heat of fusion per unit mass
L_v	latent heat of vaporization per unit mass
M	mass of a system; morphological number
$\mathcal{M}_J$	molecular weight of species J
m_ℓ, m_s	slopes of the liquidus and solidus curve (mass fractions)
$[\boldsymbol{N}^e]$	element shape functions in FEM
N_0	Avagadro's number, 6.02×10^{23} atoms mol^{-1}
N_C	number of components
N_F	number of degrees of freedom for phase equilibria
N_I	total number of atoms of species I in a mixture
N_b	bond coordination number
N_g	number of grid points in a computational domain
N_ϕ	number of phases
n	number of moles
$\boldsymbol{n}, (n_x, n_y, n_z)$	unit vector normal to a surface and its Cartesian components
n, n_g	density of grains
n_{max}	maximum density of particles available
n_p	density of potent nucleant particles; density of pores
$\mathcal{O}(\cdot)$	order of magnitude
P	power input to a system; penalty parameter
$P(r; R_{tip})$	surface of a paraboloid of revolution (dimensional)
$\mathcal{P}(\varrho)$	surface of a paraboloid of revolution (dimensionless)
p, p_a	pressure, atmospheric pressure
p_c	probability of capture
$p(\phi)$	orientation distribution function
$\tilde{p}$, p'	intermediate pressure and pressure correction in SIMPLE algorithm
$\hat{p}$	modified pressure ($= p + \rho_0 g h$)
Q	heat input to a system
q_b	boundary heat flux
$\boldsymbol{q}$	heat flux vector
R	radius
$R_g; R_{g0}$	radius of grain; final grain radius
R_1, R_2	principal radii of curvature
$\mathcal{R}$	gas constant, 8.31 J mol^{-1} K^{-1}
$\mathcal{R}$	dimensionless radius for a spherical solid particle
$\dot{R}_q$	specific heat generation rate
R_c	radius of a critical nucleus
R_p	pore radius
R_{tip}	tip radius of a paraboloid
$\{\boldsymbol{R}\}$	residual vector
r, θ, z	cylindrical coordinates

r, θ, ϕ	spherical coordinates
r_J^I	second-order interaction coefficient between solute element I and gas element J
S	bounding surface
S, S^m, s	total, molar and specific entropy
S_{mix}^m	molar entropy of mixing
$\mathcal{S}_V, \mathcal{S}_V^{s\ell}$	solid-liquid interfacial area per unit volume
$\mathcal{S}_V^{de}$	interfacial area per unit volume for inter-extradendritic liquid
$\mathcal{S}_V^{sd}$	interfacial area per unit volume for solid-interdendritic liquid
T	temperature
$\dot{T}$	cooling rate
T_0	boundary temperature; temperature where $G_s^m = G_\ell^m$
T^*	solid-liquid interface temperature
T_b	boundary temperature
T_{col}	temperature of a columnar front
T_{eut}	eutectic temperature
T_f	equilibrium melting temperature of pure material
T_{liq}	liquidus temperature
T_{per}	peritectic temperature
T_{ref}, T_0	reference temperature
T_{sol}	solidus temperature
T_v	vaporization temperature at atmospheric pressure
$\{\boldsymbol{T}^e\}, \{\boldsymbol{T}\}$	local and global vector of nodal temperatures
t, t_c	time, characteristic time
t_f	local solidification time
t_n	time of nucleation
$\boldsymbol{t}$	surface traction vector
$\boldsymbol{u}$	displacement vector
V, V^m, v	total, molar and specific volume
V_R	volume of representative volume element
V_s, V_ℓ	volume of solid and liquid phases in representative volume element
v	scalar velocity
v_g	velocity normal to the surface of a grain
$\boldsymbol{v}$, v_i	(dimensional) velocity vector and its i^{th} component
$\mathbf{v}$, v_i	(dimensionless) velocity vector and its i^{th} component
$\mathbf{v}_K$	velocity vector for species K
v_n	normal component of velocity of the solid-liquid interface
v_{sound}	speed of sound
v_T	isotherm velocity
W	width; total work done by external forces
W_0	phase-field interface width
X_I	molar composition of species I
$\boldsymbol{X}$	material coordinate vector
$\{\mathbf{X}\}, \{\mathbf{Y}\}, \{\mathbf{Z}\}$	element vectors of nodal coordinates in FEM
$\boldsymbol{x}$	position vector
x^*	interface position in 1-D problems
x, y, z	Cartesian coordinates; also x_1, x_2, x_3
$\hat{\mathbf{x}}, \hat{\mathbf{y}}, \hat{\mathbf{z}}$	unit vectors in Cartesian coordinates

Greek alphabet

α	thermal diffusivity ($= k/(\rho c_p)$)
α, β, γ	generic phases
α_T	linear thermal expansion coefficient ($= \beta_T/3$)
β	Solidification shrinkage ($= \rho_s/\rho_\ell - 1$)
β_T	volumetric thermal expansion coefficient ($= 3\alpha_T$)
β_C	volumetric solutal expansion coefficient
β_p	coefficient of compressibility
$\Gamma_{s\ell}$	Gibbs-Thomson coefficient ($= \gamma_{s\ell} T_f/(\rho_s L_f)$)
$\Gamma^{m*}_{s,\ell}$, $\mathbf{\Gamma}^{\sigma*}_{s,\ell}$, $\Gamma^{h*}_{s,\ell}$, $\Gamma^{C*}_{s,\ell}$	interfacial mass, momentum, energy or species term for solid or liquid
$\gamma_{f\ell}$	surface energy between foreign substrate and liquid
γ_{fs}	surface energy between foreign substrate and solid
γ_{gb}	grain boundary energy
$\gamma_{s\ell}, \gamma^0_{s\ell}$	surface energy between solid and liquid; value of isotropic surface energy
Δ	dimensionless undercooling $c_p \Delta T/L_f$ (Stefan number)
ΔC_0	difference in compositions across eutectic plateau
$\Delta G_n^{homo}, \Delta G_n^{hetero}$	free energy barrier for homogeneous or heterogeneous nucleation
ΔH^m_{mix}	molar enthalpy of mixing
ΔS^m_f	molar entropy difference between solid and liquid
Δs^J_f	specific entropy of fusion of species J ($= L^J_f/T^J_f$)
ΔT	total undercooling
ΔT_b	undercooling for bridging or coalescence
ΔT_c	characteristic temperature difference
ΔT_0	Equilibrium freezing range ($= T_{liq} - T_{sol}$)
ΔT_k	kinetic undercooling
ΔT_n	nucleation undercooling
ΔT_R	curvature undercooling
ΔT_C	solutal undercooling
ΔT_T	thermal undercooling
$\Delta x, \Delta y, \Delta z$	grid spacing in various coordinate directions
δ	dimensionless solidified layer thickness; boundary layer thickness
ε_{JK}	bond energy between atoms of J and K
$\boldsymbol{\varepsilon}$	strain tensor
ε_{eq}	equivalent strain
$\varepsilon_4, \varepsilon_n$	4-fold, n-fold coefficient for the planar anisotropy of $\gamma_{s\ell}$
η	dimensionless $y-$coordinate; paraboloidal coordinate
ζ	dimensionless $z-$coordinate; fractional time step
θ	dimensionless temperature; angular coordinate; wetting angle
$\bar{\kappa}$,κ_G	mean and Gaussian curvature of a surface
Λ	ratio of eutectic spacing to extremum value ($= \lambda/\lambda_{ext}$)
λ	wavelength of instability; eutectic spacing
λ_1, λ_2	primary, secondary dendrite arm spacing
μ_ℓ	shear viscosity of a Newtonian fluid
$\mu_{J\alpha}$	chemical potential of species J in phase α

μ_k	kinetic attachment coefficient
ν_ℓ	kinematic viscosity ($= \mu_\ell/\rho_\ell$)
ν_0	atomic vibration frequency
ν_e	Poisson's ratio
ξ	dimensionless $x-$coordinate; parabolic coordinate
$\boldsymbol{\xi}$	Cahn-Hoffmann vector ($= \nabla(r\gamma_{s\ell}(\boldsymbol{n}))$)
π	$3.14159\ldots$
Π	dimensionless scaled pressure
ρ	density
ρ_0	density at reference temperature and pressure
ϱ	dimensionless radial coordinate
$\boldsymbol{\sigma}$	total stress tensor
$\hat{\boldsymbol{\sigma}}$	effective stress tensor ($= \boldsymbol{\sigma} + p\boldsymbol{I}$)
σ_{eq}	equivalent stress
σ^*	dendrite tip selection constant
σ_n	instability growth rate exponent for mode n
σ_y	yield stress
$\boldsymbol{\tau}$	extra stress tensor
τ	dimensionless time
τ_0	time scale factor in phase-field model
Υ	noise in phase-field equation
ϕ	constant used to describe interface position
ϕ_s, ϕ_ℓ	existence function for solid, liquid phase
χ_α	mole fraction of phase α
ψ	phase-field order parameter
Ψ	surface stiffness
Ω^m	regular solution parameter
Ω	supersaturation
$\boldsymbol{\omega}$	vorticity vector ($= \nabla \times \boldsymbol{v}$)

Subscripts, superscripts and indices

A^*	evaluated on the solid-liquid interface
A_C	composition
A_c	characteristic value
A_{col}	columnar zone
A^{el}	elastic deformation
A_{eut}	eutectic
A_ℓ	liquid phase
A_g	gas phase
A_k	attachment kinetics
A_I, A_J	species I, species J
A_{liq}	liquidus
A^m	amount per mole
A_n	component of vector A normal to the interface
A_p	pores
A^R	surface with radius of curvature R
A_s	solid phase
A_{sol}	solidus
$A_{s\ell}$	solid-liquid interface

A^{th}	thermal deformation
A^{tr}	transformational deformation
A^{vp}	viscoplastic deformation
$A_\alpha, A_\beta, \ldots$	quantity in phase α, β, ...
A_x, A_y, A_z	x, y, z components of a vector
A_0	nominal or reference value
A^∞	flat surface ($R \to \infty$)

Mathematical functions

Symbol	Meaning	Representation
$\mathrm{E}_1(u)$	exponential integral	$\int_u^\infty \frac{e^{-s}}{s} ds$
$\mathrm{erf}\,(u)$	error function	$\frac{2}{\sqrt{\pi}} \int_0^u e^{-s^2} ds$
$\mathrm{erfc}\,(u)$	complementary error function	$1 - \mathrm{erf}\,(u)$
$f(\theta)$	nucleation geometric factor	$\frac{(2+\cos\theta)(1-\cos\theta)^2}{4}$
$\mathcal{L}_n(x)$	Laguerre polynomial	$\frac{e^x}{n!}\frac{d^n}{dx^n}\left(e^{-x}x^n\right)$
$P_{nm}(x)$	associated Legendre polynomial	$\frac{(-1)^m}{2^n n!}\left(1-x^2\right)^{m/2}\frac{d^{n+m}}{dx^{n+m}}\left(x^2-1\right)^n$
Q_4	first cubic harmonic function	$n_x^4 + n_y^4 + n_z^4$
S_4	second cubic harmonic function	$n_x^2 n_y^2 n_z^2$
$Y_{nm}(\theta,\phi)$	spherical harmonic function	$\sqrt{\frac{(2n+1)(n-m)!}{4\pi(n+m)!}} e^{-im\phi} P_{nm}(\cos\theta)$
$\delta(x)$	Dirac δ-function	$\delta(x) = \begin{cases} +\infty & x = 0 \\ 0 & x \neq 0 \end{cases}$ $\int_{-\infty}^{\infty} \delta(x)dx = 1$
δ_{ij}	unit tensor (Kronecker delta)	$\delta_{ij} = \begin{cases} 1 & i = j \\ 0 & i \neq j \end{cases}$
ε_{ijk}	permutation tensor	$\begin{cases} 1 & i,j,k \text{ even permutations} \\ -1 & i,j,k \text{ odd permutations} \\ 0 & \text{otherwise} \end{cases}$

Mathematical operators

Symbol	Meaning	Representation
$\boldsymbol{A} \cdot \boldsymbol{B}$	dot product of two vectors	$a_i b_i$
$\boldsymbol{A}^T$	transpose of a second rank tensor	a_{ji}
$\boldsymbol{A} : \boldsymbol{B}$	scalar product of second rank tensors	$a_{ij} b_{ji}$

$D\psi/Dt$	material derivative of ψ	$\dfrac{\partial \psi}{\partial t} + (\boldsymbol{v} \cdot \nabla)\psi$
$\mathrm{tr}\boldsymbol{A}$	trace of a second rank tensor	a_{ii}
∇A	gradient of a scalar	$\dfrac{\partial A}{\partial x_i}$
$\nabla \cdot \boldsymbol{A}$	divergence of $\boldsymbol{A}$	$\dfrac{\partial a_i}{\partial x_i}$
$\nabla \times \boldsymbol{A}$	curl of a vector	$\varepsilon_{ijk}\dfrac{\partial a_j}{\partial x_k}$
$\nabla^2 A$	Laplacian of A	$\dfrac{\partial^2 A}{\partial x_i \partial x_i}$
$\|\boldsymbol{A}\|$	L_2 norm of a vector	$\sqrt{a_i a_i}$
$\langle A \rangle$	volume average of A	$\dfrac{1}{V_R}\displaystyle\int_{V_R} A \, dV$
$\langle A_{s,\ell} \rangle$	phase average of A_s or A_ℓ	$\dfrac{1}{V_R}\displaystyle\int_{V_R} \phi_{s,\ell} A \, dV$
$\langle A \rangle_{s,\ell}$	intrinsic average of A_s or A_ℓ	$\dfrac{1}{V_{s,\ell}}\displaystyle\int_{V_R} \phi_{s,\ell} A \, dV$
$\left\langle A^*_{s,\ell}\boldsymbol{n} \right\rangle^*$	interfacial average of A_s or A_ℓ	$\dfrac{1}{A_{s\ell}}\displaystyle\int_{A_{s\ell}} A^*_{s,\ell}\boldsymbol{n} dA$
$\langle C \rangle_M$	mass average composition	$\displaystyle\int_0^{f_s} C_s df_s + \int_0^{f_\ell} C_\ell df_\ell$

Classical dimensionless numbers

Name	Expression	Physical Meaning
Biot	$\mathrm{Bi} = \dfrac{h_T L_c}{k}$	ratio of heat advection from a surface to heat conduction inside
Boussinesq	$\mathrm{Bo} = \dfrac{g\beta_T \Delta T_c L_c^3}{\alpha_0^2}$	ratio of heat advected by buoyancy to conducted heat
Fourier	$\mathrm{Fo} = \dfrac{\alpha t_c}{L_c^2}$	ratio of characteristic time t_c to the time for conduction L_c^2/α
Grashof	$\mathrm{Gr} = \dfrac{g\beta_T \Delta T_c L_c^3}{(\mu_\ell/\rho_{\ell 0})^2}$	ratio of buoyant advective flow to viscosity
Lewis	$\mathrm{Le} = \dfrac{\alpha}{D}$	ratio of thermal diffusion to mass diffusion
Péclet	$\mathrm{Pe} = \dfrac{v_c L_c}{\alpha}$	ratio of heat advection to heat conduction
Péclet (solutal)	$\mathrm{Pe}_C = \dfrac{v_c L_c}{D}$	ratio of solute advection to solute diffusion
Prandtl	$\mathrm{Pr} = \dfrac{c_p \mu_\ell}{k} = \dfrac{\nu_\ell}{\alpha}$	ratio of momentum and thermal diffusivities in a fluid

Rayleigh	$\mathrm{Ra} = \dfrac{\rho_0 g \beta_T \Delta T_c L_c^3}{\mu_\ell \alpha_0}$	ratio of buoyant advection to the product of viscosity and heat conduction
Reynolds	$\mathrm{Re} = \dfrac{\rho v_c L_c}{\mu_\ell} = \dfrac{v_c L_c}{\nu_\ell}$	ratio of inertia to viscosity
Schmidt	$\mathrm{Sc} = \dfrac{\mu_\ell}{\rho_\ell D_\ell} = \dfrac{\nu_\ell}{D_\ell}$	ratio of momentum diffusivity to mass diffusivity
Stefan	$\mathrm{Ste} = \dfrac{c_p \Delta T}{L_f}$	ratio of sensible heat to latent heat

CHAPTER 1

OVERVIEW

1.1 Introduction

Solidification processes are familiar to all of us, whether they concern the formation of frost on windows or ice in trays, the freezing of solders in electronic circuits, or the casting of aluminum and steel in industrial practice. Solidification has long represented a major force in human development, and some of the "Ages" of man have even been classified by the alloys that the inhabitants were able to melt and cast. During the Bronze Age, ca. 4000 BC - 1200 BC, copper-based weapons and other artifacts of daily life were common throughout Europe and Asia. Examples are shown in Fig. 1.1(a). However, once it became possible to melt and alloy iron, ca. 1200 BC, this metal quickly replaced bronze for weapons and other applications because of its superior properties. Figure 1.1(b) shows an Iron Age axe. Several variants of steel, the most famous of which is the legendary Damascus steel, were produced in antiquity by mechanical means.

The invention of the Bessemer process in 1858 led to the mass production of steel in liquid form, which was then cast into shapes and ingots for wrought processing. This was one of the key inventions of the industrial revolution, and provided the foundation for transportation by rail, and later by automobile. Similarly, the Hall-Héroult process for producing aluminum, invented in 1886, enabled the mass production of aluminum cast products, which in turn gave rise the aircraft industry in the following century.

The ability to produce these metals in liquid form made it possible to easily manufacture alloys of controlled composition, which could then be cast into either final products or into ingots that, in turn, would be deformed in the solid state into plates, sheets, billets, and other wrought products. The solidification process marked the stage of production where the composition and structure were set for all future processing. Through the first half of the 20^{th} century, metallurgists developed an understanding of how the properties of cast products were related to the conditions extant during the solidification process.

One could argue that the art and practice of solidification entered the

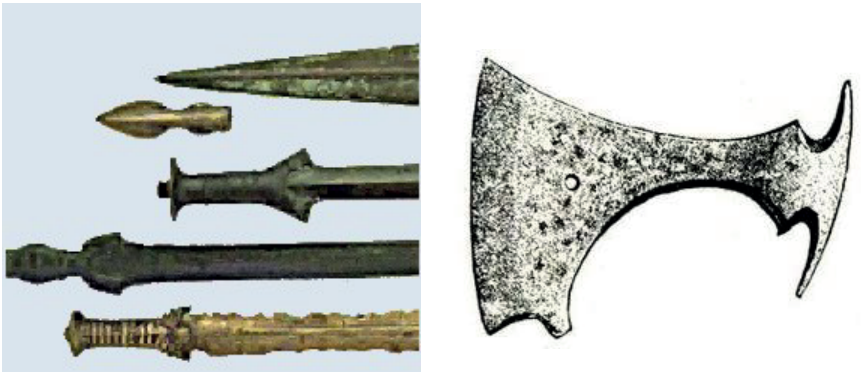

(a) (b)

Fig. 1.1 (a) Bronze age weapons (Reproduced with permission from images. encarta.msn.com); (b) Iron age axe (Photograph taken by Glenn McKechnie, April 2005).

realms of engineering and science with the publication of Chalmers' landmark text *Principles of Solidification* in 1964 [7], which presented some of the basic models for solute partitioning during the freezing of alloys, and helped to explain how microstructural patterns such as dendrites evolve during planar or spherical growth. Ten years later, Flemings' *Solidification Processing* [8] extended this modeling approach to develop models for the evolution of measurable microstructural features, such as dendrite arm spacing and segregation patterns. These models began to quantify the effect of processing parameters such as the cooling rate and the temperature gradient, as well as their interaction with alloy properties such as the freezing range and the underlying phase diagram on the final structure. Over the next decade, many important advances were made in the understanding of pattern formation in solidification microstructures, in particular regarding length scales in dendritic growth. Largely as a result of these advances, Kurz and Fisher published *Fundamentals of Solidification*, which focused in greater detail on the evolution of microstructure [10].

The present book is intended to be the next entry in this line. The time since the publication of Kurz and Fisher's text has seen the advent of large scale computation as a tool for studying solidification. This has allowed significant advances to be made in both theory and application. The development of phase-field methods has permitted a further understanding of the evolution of complex microstructures, and the availability of inexpensive large-scale computers and commercial software packages now allows process engineers to perform realistic simulations of macroscopic heat transfer, solute transport and fluid flow in realistic geometries. The development of volume averaging methods and the statistical representation of microstructures provide a bridge between the microscopic and macroscopic scales. Our objective in this book is to place the models de-

scribed in these earlier texts, as well as more recently developed ones, in a context that begins with fundamental concepts and culminates in analytical and/or numerical implementations for practical applications.

The unifying theme for our approach is the classification of various phenomena over a range of length and time scales, as illustrated in Fig. 1.2. At the macroscopic length scale, geometry and processing conditions determine the progress of solidification at various locations. The figure shows as an example a six-cylinder engine block, roughly one meter in length, that freezes over a time period as long as 30 minutes. We also show the temperature distribution at a particular time, computed with a finite element simulation of the heat transfer process.

By focusing on smaller length scales, roughly between 1 μm and 1 mm, we are able to observe the *microstructure*. Figure 1.2 shows an array of dendrites, having grown from an initially planar interface into the liquid phase. The dendrites are visible because of a chemical segregation that occurs on the microscopic scale. When solidification takes place in the presence of fluid flow, solute can be advected to distances much larger than the local microscopic scale, thereby causing *macrosegregation*.

Certain processes occurring at the atomic to nanometer length scale are also important for solidification. The properties of the solid-liquid interface, and the manner in which atoms attach to it, can affect the growth patterns. For example, the anisotropy of the surface energy determines to a large extent the morphology of the dendrite patterns observed at the microscopic scale.

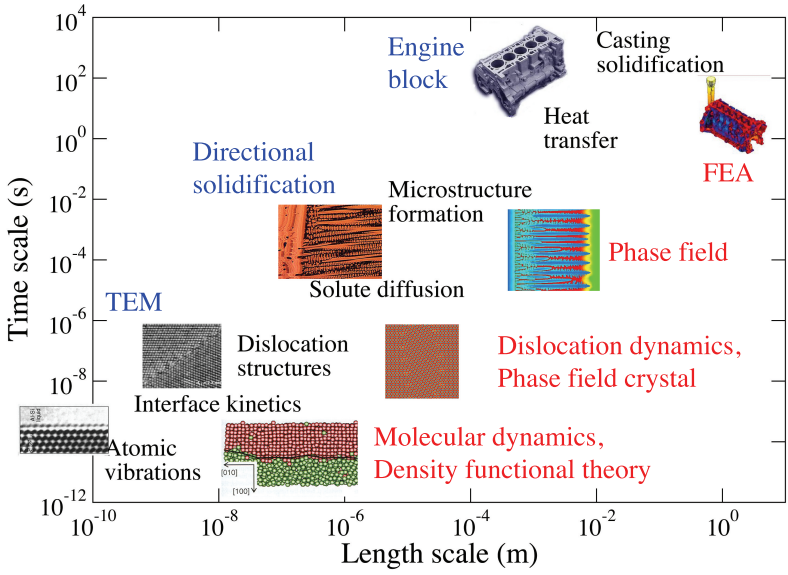

Fig. 1.2 A schematic illustration of the various phenomena associated with solidification at various length and time scales.

1.1.1 Organization of the text

We begin our book with the present overview chapter, which concludes with a section describing various solidification processes. These are presented in sufficient detail for the reader to understand the important aspects of each process, and in order to motivate the remainder of the book. A deeper treatment is left to others.

The rest of the book is divided into three parts: *Fundamentals*, *Microstructure* and *Defects*. Fundamentals, as its name implies, provides the basic principles needed to study solidification. We begin with Chap. 2, *Thermodynamics*, in which the concepts of equilibria for condensed phases, including models for the free energy and chemical potential, are developed. We also introduce departures from equilibrium, including the effect of curvature, and kinetics. These concepts are then used in Chap. 3, *Phase Diagrams*, to motivate and study equilibrium phase diagrams in binary and ternary systems as the result of chemical equilibria between phases.

Equilibrium implies that the processes take place over sufficient time for there to be no spatial variations in temperature, composition, pressure, etc. Thus, there exists no effective time or length scale in equilibrium. The finite time associated with real processes, however, leads to spatial variations over length scales that affect the properties of the solidified part. The microstructure shown in the previous section are prime examples. The governing equations for transport of mass, momentum, energy and species are developed in Chap. 4 for this purpose. In particular, we derive governing equations for single phases, and for the interface between phases. We also develop volume-averaged forms appropriate for control volumes that contain a mixture of solid and liquid phases. This latter formulation is extremely useful in subsequent chapters for developing mesoscale models that bridge the microscopic and macroscopic length scales.

The focus of this book is on solidification processes, which are characterized by a moving boundary between the solid and liquid phases. This represents a modeling challenge, as one must apply boundary conditions on a phase boundary whose position is *a priori* unknown. Chapter 5 is devoted to the study of the class of such problems that have an analytical solution. These problems are very useful in identifying the important physical phenomena that control solidification processes. In order to go beyond these model problems, which are mostly one-dimensional and also require constant material properties and simple boundary conditions, numerical methods are required. These are developed in Chap. 6.

With these fundamentals in hand, we proceed to Part II, the study of microstructure. Continuing the theme of organizing by length scale, we begin with Chap. 7, *Nucleation*, in which we explore how the first solid forms from the melt as it cools. Thermodynamics play a crucial role, and we see that the sub-microscopic length scale for nucleation is set by the balance between surface energy associated with the solid-liquid interface and free energy associated with the bulk phases. As such nuclei grow to microscopic size, they begin to express their underlying crystallography.

The most common morphology is that of the dendrite, studied in detail in Chap. 8. The length scale associated with dendrites is very important for the use of cast products since it strongly influences their properties, as well as the formation of defects. We therefore expend some effort to investigate how the length scales are affected by processing. We present the analyses in some detail so that the interested reader can appreciate the underlying theory, but we also emphasize the key results that are needed in subsequent chapters. In Chap. 9, we study eutectic and peritectic alloy systems, in which the solidification involves the melt and two distinct solid phases. We focus in particular on the evolution of length scales in the microstructure of these alloys as it is affected by processing conditions.

These chapters identify processes that lead to chemical segregation in the final product. The amount and extent of this segregation affects the material properties, and is important to understand for subsequent heat treatment (e.g., homogenization and precipitation). Models for this phenomenon are presented in Chap. 10, and constitute direct applications of the principles developed in Chaps. 5 and 6 at the microscopic scale. We conclude this part of the book with Chap. 11, Macro-micro modeling, which shows how to integrate the models for microstructure developed in Chaps. 7-10 with the macroscale modeling methods developed in particular in Chap. 6. This provides a powerful tool for the analysis of real casting processes.

Finally, in Part III we present a detailed analysis of some of the most common defects found in solidified parts. Chapter 12, *Porosity*, describes how solidification shrinkage and the evolution of dissolved gases lead to porosity in the final product. Almost all materials increase their density upon freezing, with water and semiconductors such as silicon and germanium being well-known exceptions. As solidification proceeds, liquid flow is needed to compensate for the volume change upon freezing. This flow is opposed by viscous forces exerted by the microstructure, and if the impediment is large enough, pores can develop. If, in addition to the viscous effects, there are superimposed strains, e.g., from thermal contraction of the solid, then hot tears can form; a phenomenon explored in Chap. 13. Finally, in Chap. 14, *Macrosegregation*, we demonstrate how relative movement of the solid and liquid can lead to segregation on the macroscopic scale.

1.2 Solidification processes

1.2.1 Shape casting

Casting is the most cost-effective way for manufacturing parts of complex shape. Applications range from mass-produced automotive parts (blocks, cylinder heads, suspension and brake components, etc.), to individual products such as jewelry and statuary. All of these processes have in common a mold with a cavity corresponding to a “negative” of the final product, which is initially filled by liquid, after which solidification takes place by

Table 1.1 Process characteristics for shape casting.

Process	Mold material	Cavity	Core materials
Foundry casting	Bonded sand	Wood, metal pattern	Baked sand
Investment casting	Fired ceramic	Wax, polymer	Leachable ceramic
Permanent mold and die casting	Tool steel, Copper, Graphite	Machined cavity	Metal

heat extraction through the mold. The processes differ mainly in the mold material and how the cavity is formed, as listed in Table 1.1. Each of these processes is described in more detail in the following sections.

Foundry casting

Foundry casting, sometimes called sand casting, is one of the most common processes for mass production of parts with complex shapes. A re-usable pattern is made from wood, metal, or other suitable materials. The pattern has the shape of the intended part, augmented in several ways to accommodate the solidification process. For example, the part dimensions are increased by a "shrink factor" that compensates for the volume change (typically a few percent) associated with thermal contraction during cooling from the solidification temperature to room temperature. The pattern may also have to differ from the desired final product in order to allow it to be easily removed from the mold before casting, as well as the addition of risers to compensate for solidification shrinkage and gating to conduct the liquid metal into the mold.

The mold, illustrated in Fig. 1.3, is formed in a *flask*, which generally consists of two parts: the lower *drag* and the upper *cope*. In a typical hand-molding operation, the drag part of the pattern is placed on a flat surface, and the drag case is inverted over it. A sand mixture is then poured over the pattern and compacted until it has sufficient strength so as to hold together after the pattern is removed. A typical composition (by weight) for the molding sand is 96 parts silica sand, 4 parts bentonite (clay) and 4 parts water. The particle size is controlled by sieving the mixture. After formation of the drag, it is inverted and the cope is fitted to it. The cope part of the pattern is then connected to the drag part. A parting compound, e.g., ground bone, is sprinkled onto the surface and the cope is filled with sand and compacted. The two mold halves are subsequently separated and the pattern is removed, thus forming the mold cavity. The cope may be formed separately after which the two halves are assembled. This is the more typical approach in automated processes. After the pattern has been removed, *cores* can be placed in the mold cavity to produce passages inside the final cast product. One can usually discern the *parting line*, corresponding to the location of the joint between the cope and drag on the

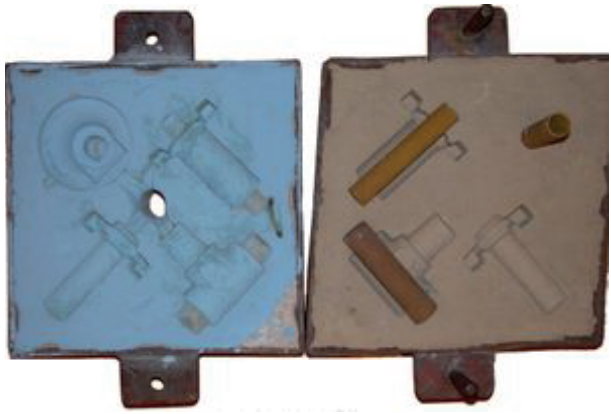

(a)

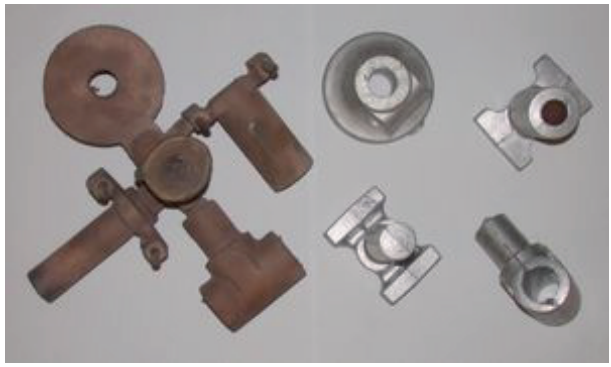

(b)

Fig. 1.3 (a) A sand mold for the manufacturing of simple cast parts. Cores have been placed in the drag to create internal cavities in the cast product. Notice the hole in the center of the cope corresponding to the down-sprue, and the runners from the central sprue to the individual castings. (b) Bronze and Al castings obtained with this mold. (Source: en.wikipedia.org/wiki/Sand_casting [4].)

surface of the casting.

In addition to the part pattern, the mold must also have the "plumbing" to allow metal to fill the mold cavity. As illustrated in Fig. 1.3, this consists of a basin to absorb the impact of pouring, a down-sprue to conduct metal to the level of the mold cavity, and a set of runners and in-gates to feed the metal into the cavity. The main objectives of this *feeding system* is to introduce the liquid into the cavity with as little turbulence as possible, so as to avoid incorporating surface oxides and other undesirable impurities into the casting. The sand mold is porous, allowing air to escape readily during filling. The runner system may also incorporate a ceramic filter in order to capture undesirable materials, such as oxide films and stray sand particles before they enter the mold. In addition to the runners

and in-gates, most castings also have *risers* that are strategically placed on the casting. These provide additional metal to feed solidification shrinkage, which would otherwise lead to internal cavities in the solidified part. For a more detailed description of the practical requirements of the feeding system, the reader is referred to the texts by Heine, et al. [9] and by Campbell [5]. After the mold cavity is filled and the part solidifies by heat extraction into the mold, the sand mold is broken away, leaving the final casting.

Heat is extracted from the metal by the cold mold, thus effecting solidification. Although methods and results for the analysis of this heat transfer problem are discussed in Chaps. 5 and 6, a brief, more general discussion is useful at this point. The heat removed from the casting includes both the *sensible heat*, as measured by the specific heat c_p, and the latent heat of fusion L_f. In most materials, the latent heat contribution is much larger than the sensible heat. The latent heat flows through the solidified region of the casting, across the solid-mold interface and into the mold. It is demonstrated in Chap. 5 that, for sand casting, the overall heat transfer is dominated by heat conduction in the mold. It is moreover found that the solidified thickness x^* as a function of time t for a pure metal can be approximated by

$$x^* \approx \frac{2(T_f - T_0)}{\rho_s L_f \sqrt{\pi}} \sqrt{k_m \rho_m c_{pm}} \sqrt{t} \tag{1.1}$$

where T_f is the equilibrium freezing temperature of the metal, T_0 is the initial temperature of the mold, ρ_s is the density of the solid metal, k_m is the thermal conductivity of the mold, ρ_m is the density of the mold material, and c_{pm} is its specific heat. In the case where heat transfer is dominated by the mold, this result can be generalized by replacing x^* by the ratio of the volume V of the part to its surface area A. When inverted to obtain an expression for the solidification time t_f, the result is called *Chvorinov's Rule*:

$$t_f = \frac{\pi}{4 k_m \rho_m c_{pm}} \left(\frac{\rho_s L_f}{T_f - T_0} \right)^2 \left(\frac{V}{A} \right)^2 \tag{1.2}$$

Chvorinov's rule is used in daily foundry practice to estimate the solidification time for parts. It can be further extended to assess the solidification pattern in parts with varying section sizes, and thus predict the overall progress of solidification through the part. Casting designers can then place risers appropriately to ensure that the last regions to freeze, where shrinkage porosity is likely (see Chap. 12), are situated outside the final product. In many cases, this simple calculation is sufficient for designing an acceptable casting. However, many castings are either too complicated, or require too much precision, for this approximate approach to be adequate, and in these cases computer simulations of the filling and heat transfer are carried out, using the methods described in Chap. 6.

Before leaving this topic, we should mention an interesting variant of the foundry casting process known as *lost foam casting*. In this procedure, the pattern is constituted of foamed polystyrene, and is left in the mold during casting. The heat of the incoming metal vaporizes the polystyrene, with the gases escaping through the mold. This process offers several advantages. Since the pattern does not need to be removed from the mold, there is more flexibility in the pattern design. Similarly, since the mold does not have to be manipulated to remove the pattern, unbonded sand can be used to form it, thus reducing the cost of reprocessing the sand between uses.

Investment casting

Sand casting is an excellent technique for mass production of complex shapes. There are some applications, however, where the need for a superior surface finish or more controlled solidification conditions leads to the use of the *investment* or *lost wax* casting process. This process is more expensive than sand casting, and is for this reason used most often in applications where the material itself is costly, or where the final shape is very difficult to obtain by machining. Examples include gold and silver jewelry, bronze sculptures, titanium parts for medical or sporting applications, and superalloy components for high temperature engine applications.

The pattern is made from a material with a low melting temperature such as plastic or wax, which is then coated with ceramic to form a mold. The ceramic can be simply cast around the pattern, e.g., from plaster of Paris, or built up as a series of layers. The first layer, i.e., the one closest to the part, is usually fabricated from a low viscosity slurry with fine particles so that the ceramic can penetrate into intricate designs on the pattern, and provide a good surface finish to the cast component. This layer is then strengthened by having sand sprinkled over it. After partial drying, the "invested" pattern/mold combination is dipped into a low viscosity slurry and then coated again with sand. The process is repeated until a thick, strong mold has been created. The mold/pattern is subsequently heated to melt the wax pattern material, which is then poured out of the mold, leaving a cavity of the desired shape. The ceramic mold is ultimately fired to achieve final strength. Ceramic cores can be incorporated by forming the wax pattern around them before investing the pattern into the mold.

The casting is obtained by pouring the melt into the ceramic mold. The mold is usually pre-heated to reduce thermal stresses during filling, and to ensure that the melt flows into intricate details of the mold before freezing. In some cases, thermal insulation is applied at certain locations on the mold to ensure a desirable heat flow pattern during solidification. The filling and solidification is sometimes done under vacuum to ensure that all of the air is removed from the mold, and to prevent contamination of the melt during filling. In that case, the heat transfer is controlled by radiation from the mold assembly to the environment. If a hollow casting is desired, the mold may be inverted a short time after pouring so as to

decant the remaining liquid. After completion of solidification, the ceramic mold is broken off the casting. In some cases, internal cores are removed by dipping the casting in a caustic solution to dissolve the core. Figure 1.4 shows an example of a turbocharger rotor made by investment casting.

Fig. 1.4 Left to right: A ceramic mold after removal of the pattern; a superalloy turbocharger rotor (etched to reveal grain structure); and a half-section of a ceramic mold. Notice the smooth ceramic at the casting surface, giving way to a coarser consistency.

Another example of an industrial application is the production of superalloy blades for turbine applications. When in service, the blades are subjected to the high combustion temperature in the engine as they rotate at high speed. This produces a tensile stress directed along the axis of the blade, and the predominant failure mechanism occurs by creep deformation along grain boundaries. For this reason, the best solidification microstructure is one where all grain boundaries are aligned with the blade axis, or even better, where there are no grain boundaries at all, i.e., a single crystal. To achieve this microstructure, the casting is solidified by placing the mold assembly in a furnace that maintains a large temperature gradient, and then slowly withdrawing the mold assembly through the furnace to obtain *directional solidification*. Figure 1.5(a) shows an example of a cast turbine blade. Notice that the blade has a "pigtail" at the bottom serving to select only one grain from the many that form at the lowermost chill plate, thus producing a single crystal in the blade. The process by which the grains are eliminated is described in detail in Chap. 11, where we present methods for simulating the microstructure. An example of a result from such a simulation is given in Fig. 1.5(b). In this particular case, a stray grain has formed at the bottom blade platform above the pigtail and grown into the blade, producing a bicrystal, which would be cause for rejection during inspection.

Permanent mold and die casting

In the processes described in the previous sections, each casting had its own mold, which was destroyed after solidification in order to recover the cast part. Some parts lend themselves to production in a re-usable mold,

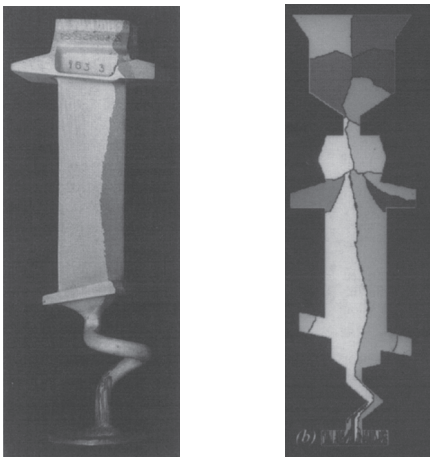

(a) Photograph of a turbine blade

(b) Simulated microstructure for this part

Fig. 1.5 A defective single crystal superalloy turbine blade, and a simulation of the microstructure formed during the casting process.

made of tool steel, copper, or graphite, depending on the application. Such parts tend to be somewhat less complex, especially with respect to any internal passages. The mold normally consists of several parts that are coated with a slurry (e.g., a suspension of graphite in alcohol), preventing the metal from reacting with the mold, as well as assisting in releasing the part after solidification. The mold parts are then assembled prior to casting. Since the mold is re-used, this process is called *permanent mold casting*. The mold may have internal heating and cooling passages to control the solidification pattern. The casting is carried out by filling the mold, waiting long enough to allow the solidification to take place, and then disassembling the mold in order to retrieve the casting. The need to disassemble the mold places some obvious limitations on the complexity of the shapes that can be cast with this process. Note that in this case, the mold is not permeable to air, and some allowance must be made for venting the air from the mold during filling.

The heat transfer characteristics in permanent mold casting are somewhat different from those in sand casting. In the latter two processes, heat transfer is determined almost exclusively by conduction through the mold. This allows the use of Chvorinov's rule to estimate the solidification time. In permanent mold casting, however, the conductivity of the mold and casting are of similar magnitude, and the dominant resistance to heat transfer is the interface between the mold and metal part. In this case, it can be assumed that the mold is maintained at temperature T_0 and that the casting is approximately isothermal at the freezing temperature T_f. One can estimate the rate of solidification by equating the heat flux across

the metal-mold interface to the rate at which latent heat is evolved by solidification. In such a case, the thickness of the solidified layer becomes

$$x^* = \frac{h_T(T_f - T_0)}{\rho_s L_f} t \tag{1.3}$$

where h_T is the heat transfer coefficient at the metal-mold interface, and the other terms have the same meaning as in Eq. (1.1). Notice that, in this case, the thickness solidified is proportional to time, rather than proportional to the square root of time as in Eq. (1.1). Chvorinov's rule *cannot be used* to analyze casting processes where the solidification rate is controlled by heat transfer across the mold-metal interface. We should note that h_T depends strongly on thermal strains, which can affect the size of the air gap between the metal and mold. This is detailed further in Chaps. 4 and 13.

Another casting process that uses a permanent mold is *die casting*. The distinction between the two processes is that, in permanent mold casting, any pressure that is applied tends to be low, whereas in die casting, liquid metal is injected at high speed and high pressure into a die, usually made of tool steel. The process is very similar to injection molding of polymers. The reader may have seen such a process at a museum, for the manufacturing of souvenirs. Die casting is of course done at higher temperature for most metals, and at higher pressure, as well. In a typical process, the dies are coated with a release agent, and then closed. A sufficient charge of liquid is poured into a receptacle outside the die, known as a "shot sleeve," after which the charge is injected under high pressure into the die cavity. The dies are typically cooled via internal air and/or water passages. After solidification, they are opened and the part is ejected.

Die casting is used for relatively thin-walled parts, and the production rate can be quite high, making it very cost-effective for high volume production. Liquid metals tend to have a high surface tension and low viscosity in comparison to polymers. As a result, the incoming stream has a tendency to separate, or even atomize during filling, which leads to defects such as porosity and entrained oxides in the final part. This limits the applications where die casting can be used to those where mechanical properties such as fatigue resistance are not too demanding. Figure 1.6 shows sample parts for automotive use: an aluminum alloy engine cover and a magnesium alloy cross beam that serves as a lightweight support for an automobile dashboard. These parts illustrate the remarkable complexity of products achievable with this process. A variant of the process, called *low-pressure die casting*, is used to produce automotive wheels. The mold is assembled above a holding furnace, and the furnace is then sealed and pressurized to force liquid up into the die. The filling tends to produce much less agitation than high-pressure die casting.

In another variant of the process, known as *thixocasting*, the charge is semi-solid, rather than liquid. The name derives from the term *thixotropic*, which signifies that the viscosity of the material decreases with

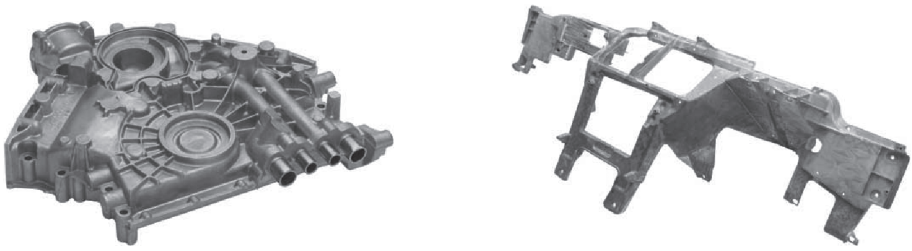

(a) (b)

Fig. 1.6 Examples of die cast parts. (a) An aluminum alloy engine cover. (b) A magnesium alloy automotive dashboard support. (Source: diecasting.org/castings.)

time while undergoing shear. Many metal alloy systems demonstrate this property since the structure can evolve to accommodate the deformation. The process has several advantages, the primary one being that the metal shows much less tendency to atomize during injection as a result of the viscosity of the semi-solid being much higher than that of the corresponding liquid. Further, the fact that the charge is only partially liquid reduces the amount of heat that has to be extracted from the dies. The principal problem in thixocasting is that the cost of preparing semi-solid materials with an appropriate microstructure can offset other advantages.

1.2.2 Continuous and semi-continuous casting

The casting processes described in the previous section are used for fabricating parts that are intended to be used essentially in their as-cast condition, perhaps after some machining and heat treatment. Other applications, such as sheets, rails, tubes, etc. are more practically produced by first casting a relatively simple form (slabs and billets) and then mechanically deforming it into the desired shape, using processes such as rolling and extrusion. We note that the alloys used for these applications, called *wrought alloys*, tend to have much lower solute contents than their counterparts used for shape casting. These products were once made by casting large quantities of metal into molds that consisted of holes dug in the ground, then removing them and performing the necessary mechanical treatments. The drawbacks of this process include very long solidification times (a matter of days for some very large ingots), and a tendency to produce separation of solute elements over very large distances in the ingot, a process called *macrosegregation*, described in Chap. 14.

Large ingot casting for subsequent mechanical processing has largely been supplanted by *continuous* or *semi-continuous casting*. In such processes, a metal is introduced into a water-cooled mold with an open exit. The process begins with a starter block in the mold exit. The metal is then introduced into the mold through a nozzle, where it proceeds to

freeze against the mold and the starter block. The block is subsequently withdrawn at a controlled rate and metal is continuously fed to maintain a constant level in the mold. This process is used to produce steel, aluminum, copper and other alloys for wrought applications, and the particular form of the continuous casting process depends to a certain extent on the material being cast.

More than 90% of the world's steel production is manufactured by continuous casting. A typical apparatus for making slabs is illustrated in Fig. 1.7(a). Liquid steel is fed from the melting units into a *tundish*, from which it is conducted into the water-cooled copper mold by a submerged entry nozzle (SEN). Typical mold dimensions are 5-25 cm by 0.5-2 m, and the casting speed for conventional slabs is 1-8 m min^{-1}. The steel is cast vertically, and as the slab exits the mold, a series of rolls gradually turns it to the horizontal direction over a distance of about 10 m. This is possible because of the low thermal conductivity and high casting speed typical of

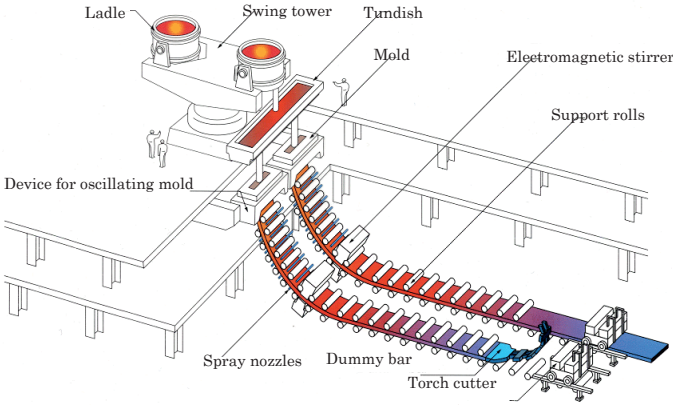

(a) A steel slab casting facility (Reproduced with permission from JFE 21st Century Foundation).

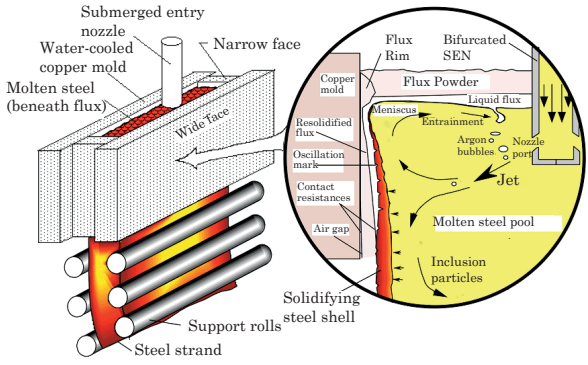

(b) A schematic of phenomena in the mold (Reproduced with permission from B. G. Thomas).

Fig. 1.7 A schematic view of a facility for continuous casting of steel slabs, and the phenomena that occur in the casting mold.

steels, which also have sufficient ductility for the bending operation. Once the steel is entirely solid, it can be cut on the fly into convenient lengths for subsequent processing. Many of the important phenomena that occur in the mold are illustrated in the close-up view shown in Fig. 1.7(b). A slag layer covers the liquid steel in the mold to protect it from oxidation. The mold is oscillated as the slab is withdrawn to help prevent sticking of the slab to the mold wall. This draws the slag into the region between the slab and the mold. It is clear from the illustration that only a small portion of the slab solidifies before the slab leaves the mold. The remaining solidification takes places below the mold by the application of water sprays between the guide rolls.

The heat transfer process in the mold is the result of several competing phenomena. We show in Chap. 4 that one can estimate the relative importance of conduction and advection (heat carried by the moving material) by computing the Péclet number, Pe

$$\mathrm{Pe} = \frac{V_c L_c}{\alpha} \tag{1.4}$$

where V_c is the casting speed, L_c is a characteristic length, e.g., the slab half-width, and $\alpha = k/(\rho c_p)$ is the thermal diffusivity of the steel. When employing values typical for steel continuous casting, one finds that $\mathrm{Pe} \approx 200$, which implies that conduction is less important than advection in the axial direction. For this reason, models of the process where the slab is treated as a 2D "traveling slice" moving with the casting speed are often encountered.

At the top of the slab, where solidification begins, there is a liquid flux layer between the slab and the mold, which makes for very effective heat transfer. This locally heats the mold, causing it to expand, and the cooling slab tends to shrink, ultimately resulting in an air gap that significantly reduces the heat transfer. We note that certain molds are designed with an inward taper in order to compensate for the thermal distortion. Accounting for these phenomena in an accurate process model can be complicated, due to the thermal distortion depending on the mold design, details of the roll positions below the mold, etc.

In steel casting, thermal stresses also play an important role below the mold. The solidification zone typically extends as much as 10 m below the mold. The solidified shell remains quite hot and ductile in this region, and the ferro-static pressure of the liquid sump deforms the shell outward between the containment/turning rolls, as illustrated in Fig. 1.8. The alternating bulging and compression of the shell can lead to centerline segregation in the final slab, as the composition that is drawn in and then pushed back out can change. Deformation of the solidifying solid is addressed in Chap. 13, and the associated segregation is considered in detail in Chap. 14.

The continuous casting process for aluminum alloys is performed somewhat differently than it is for steel. Aluminum is a much better conductor than steel, and aluminum alloys tend to have much lower high-temperature strength. This renders it impractical to bend aluminum

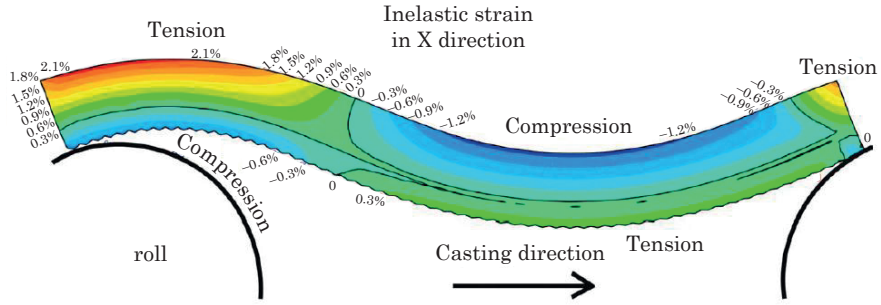

Fig. 1.8 A computer simulation of the thermal stresses that develop in a steel slab between rolls. (Courtesy B. G. Thomas).

alloys slabs, and they are therefore cast vertically into deep pits, typically 8-10 m. Such a procedure would more properly be called semi-continuous casting, but is often referred to as *direct chill* or DC casting. The molds are generally made from aluminum, and there is no mold oscillation. A mold release grease is sometimes applied before casting, or, alternatively, a continuous film of oil is fed to the meniscus that forms between the aluminum and the mold surface. Water sprays are applied below the mold to finish the solidification. DC cast aluminum slabs are typically as thick as 400-500 mm, and are cast at 60-70 mm min^{-1}. If one computes the Péclet number using these parameters, one finds that $\text{Pe} \approx 1$, which implies that the solidification process is truly three-dimensional. After the entire length of the ingot has been cast, the process is brought to a halt, the molds are removed, and the ingots are taken away for further processing. Macrosegregation and thermal stresses are significant issues in aluminum casting, but tend to be manifested in different ways than they are in the casting of steel. The geometry of the process often produces significant macrosegregation in the slabs, which can be a particularly vexing problem in some alloys. The same processes of shell solidification and air gap formation as those described for steels also occur in aluminum alloys. Thermal stresses tend to appear as distortions at the base of the ingot, and in certain severe cases, this can lead to fracture and scrapping of the entire ingot. We address this particular problem in detail in Chap. 13.

One would prefer to cast both aluminum and steel horizontally, as opposed to vertically, since this makes the plant layout more efficient. Such processes tend to be limited to rather small cross-sections, up to 100 mm or so. In a relatively recent variant of the continuous casting process, metal is poured into a fairly small gap between to rotating rolls. This process is useful for making sheets thin enough to be processed by cold rolling, which offers a significant reduction in production cost.

1.2.3 Crystal growth processes

The invention of the transistor, and the subsequent miniaturization of electronic circuits has led to a complete revolution in technology, which needs

no further description here. We note, though, that virtually all of this technology relies on the ability to produce Si crystals of extremely high quality, with very low, but at the same time well controlled, levels of impurities, and extremely low levels of mechanical defects such as dislocations. Other important applications include the fabrication of quartz and sapphire crystals for the watch industry, as well as GaAs crystals for diodes. Such crystals are grown from the melt using a variety of methods, all of which feature a high temperature gradient and small growth velocity. It is demonstrated in Chap. 8 that these conditions are required in order to maintain a stable planar interface between the solid and liquid when solutal impurities are present.

Two common crystal growth processes are illustrated in Fig. 1.9. In Czochralski growth, typically used for Si, a single crystal is produced by first preparing a large bath of a high-purity melt. A seed crystal is usually used to start the solidification process in the desired crystallographic orientation. The seed is dipped into the surface of the melt and then withdrawn upward at a controlled rate, and solidification occurs as heat is lost to the environment by radiation. The crystal and/or the crucible may be rotated during growth to minimize segregation, and to ensure that the shape is cylindrical. The principal means for heat extraction is radiation, which tends to limit the growth rate. For a 200 mm diameter crystal, the maximum growth rate is about 0.5 mm min^{-1}, which translates to the production of a 3 m long crystal in about 5 days. This is the basic process used for the preparation of a majority of the Si crystals employed in electronic applications.

In the Bridgman growth process, shown schematically in Fig. 1.9(b), a baffle separates the hot and cold zones, establishing a large temperature

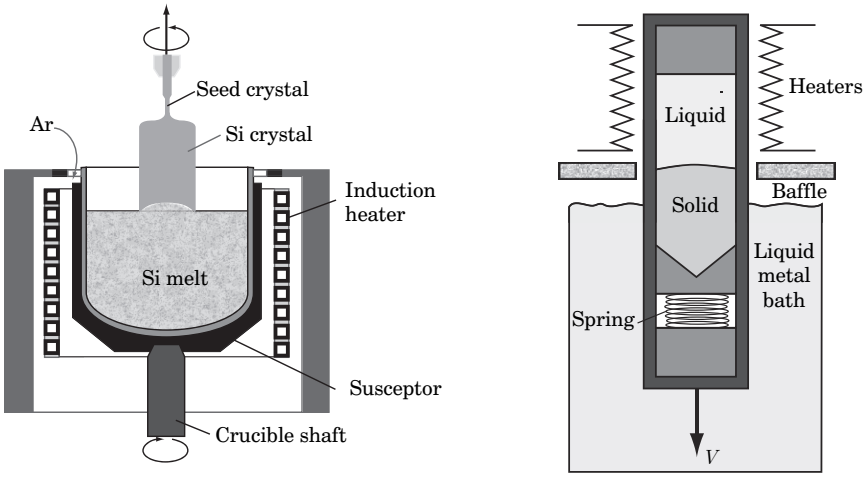

Fig. 1.9 A schematic view of (a) the Czochralski and (b) the Bridgman crystal growth processes.

gradient. The raw material for the crystal is first sealed inside a container called an ampoule, which is then placed in the hot zone of the furnace. The ampoule has a sharp point at the bottom to ensure the nucleation of only a single grain (see Chap. 7). Alternatively, there may be a seed crystal placed at the bottom of the ampoule, in which case the tip is not melted. After the material is melted, the ampoule is withdrawn at constant velocity. Once again, the objective is to produce a crystal grown under stringently controlled thermal conditions. In certain applications, the lower zone of the apparatus consists of a liquid metal bath (usually Ga) in order to give rise to the highest possible heat extraction rate. A similar process is used for directional solidification of single crystal turbine blades, as discussed previously in the section on investment casting.

Composition control is one of the most important aspects of crystal growth. Let us consider a simple application that motivates the more detailed studies of chemical segregation appearing in Chaps. 5 and 10. Suppose that there is a small amount of impurity present in the raw material, and that, upon melting, the composition of the liquid is uniform. Most materials for which this process is used demonstrate very low solubilities for impurities. As the material solidifies, the solute is rejected ahead of the interface into the liquid, gradually increasing its concentration. This problem is presented and solved in detail in Chap. 5, and we therefore limit ourselves here to a more descriptive approach to the behavior. Figure 1.10 shows the development of the composition in the solid behind, and the liquid ahead of the moving interface as it moves at constant velocity. One can see an initial solute-depleted region at the start of solidification, which eventually gives way to a steady growth region where the composition in the solid is constant. Eventually, there is also a final transient at the opposite end of the sample, where the additional solute in the boundary layer ahead of the interface is deposited. See Chap. 5 for further details. This

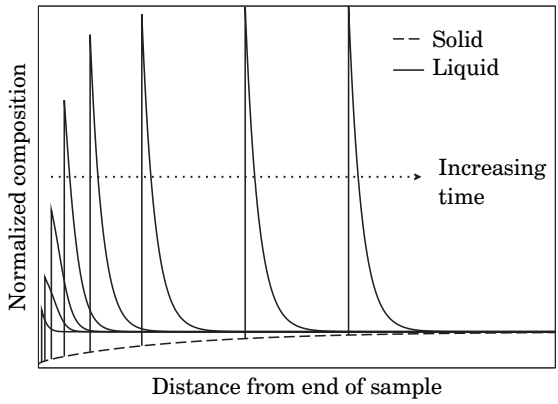

Fig. 1.10 Development of solute layer ahead of the solid-liquid interface, and the corresponding composition in the solid.

is an example of macrosegregation; i.e., separation by large distances between regions of significantly different composition.

Macrosegregation is not always a bad thing. There is a variant of the Bridgman process called *zone refining* which takes advantage of the segregation in order to create materials of high purity. Instead of melting the entire sample, zone melting consists in melting a small portion of the sample, e.g., using an induction coil, and then passing the heater over the container, moving from one end to the other. In doing so, the segregation process described above "pushes" the solute toward one end. If the process is repeated, the sample is continuously refined. This is the most common process used for preparing high purity samples of many materials.

1.2.4 Welding

One of the most common methods for joining materials is welding, in which two materials are melted by the application of some sort of directed energy, after which they re-solidify, creating a solid joint. A filler rod may also be used to help fill any gaps between the materials, or to control the chemistry of the weldment. Welding processes are often characterized by their means for melting. The most versatile method is to use an oxygen-acetylene torch; a method that is somewhat difficult to control. In arc welding, a current passing between a welding rod and the workpiece provides the necessary heat. A shielding gas or flux is used to prevent oxidation. In certain applications, the gas is ionized and forms a plasma that performs the actual energy transfer to the sample. Heat for melting can also be generated by a laser or electron beam. The energy transfer processes in welding are far more complicated than those associated with solidification, and we leave their description to other texts.

In most applications, the weld beam passes over the sample, melting the material along its path, which then re-solidifies as the weld beam moves away. Thermal stresses develop due to the large thermal gradients. One can develop a fairly simple analytical model of the process by considering the weld beam to be a point source of heat Q, traveling at constant velocity V in the $x-$direction along the surface of an infinite medium. It is convenient for a solution to transform from the Cartesian coordinate system (x, y, z) fixed on the workpiece to a reference frame (ξ, y, z) traveling with the weld beam, placed at the origin in this frame. The coordinate y measures the transverse distance from the weld centerline, and z measures the depth from the surface. Latent heat can be neglected to a first approximation, in which case the solution for the temperature field in the material is given by the so-called "Rosenthal solution"

$$T = T_0 + \frac{Q}{2\pi k r} \exp\left(-\frac{V(r+\xi)}{2\alpha}\right) \tag{1.5}$$

where T_0 is the base temperature of the material before welding, Q is the power of the heat source, k is the thermal conductivity, $\alpha = k/(\rho c_p)$ is the

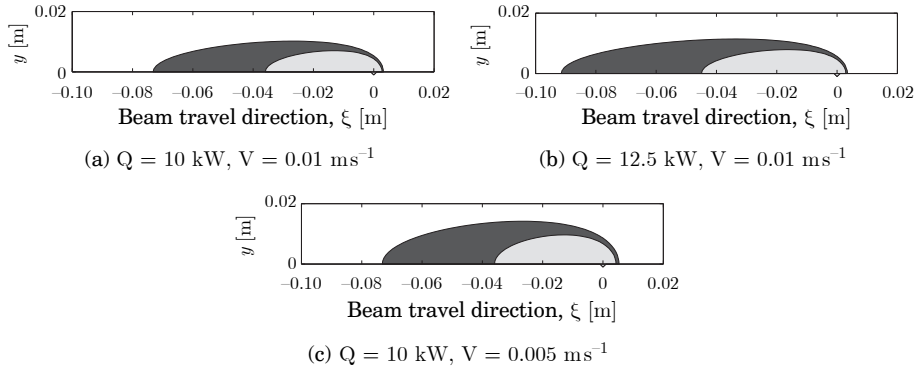

(a) Q = 10 kW, V = 0.01 ms^{-1}

(b) Q = 12.5 kW, V = 0.01 ms^{-1}

(c) Q = 10 kW, V = 0.005 ms^{-1}

Fig. 1.11 Surface temperatures computed with Eq. (1.5) for various values of the welding parameters.

thermal diffusivity, and $r = (\xi^2 + y^2 + z^2)$ is the radial distance from the weld beam. Notice that the solution is symmetric with respect to y and z, signifying that it is sufficient to consider the solution on the surface.

Figure 1.11 shows several cases obtained by varying the parameters in Eq. (1.5). In the base case, shown in Fig. 1.11(a), we set $Q = 10$ kW and $V = 0.01$ m s^{-1}. These values are appropriate for the welding of steel. The molten pool ($T > 1500°$C) is shown in light gray, and in this frame, the material moves from right to left in the figure (i.e., the weld power source moves from left to right in the laboratory frame). The weld beam is located at the origin, and one can see that the pool extends ahead of the beam, and that there is a "tail" of heated material behind it. Material that has been melted is said to be in the *fusion zone*. We also show in darker gray a portion of the material whose temperature has been raised above 800°C, roughly corresponding to the transition to austenite. The portion of the material that undergoes the solid state transformation, but is not melted, is called the *heat-affected zone* or HAZ. This region is usually weaker than the base metal or the weldment, and is thus a source of mechanical failure. The analytical expression for the temperature renders it possible to explore the importance of the process parameters on width. Figure 1.11(b) shows the same contours as the base case, after the input heat has been increased by 25%, and Fig. 1.11(c) portrays the effect of decreasing the welding speed by 50%. Both changes increase the width (and depth) of both the fusion zone and the HAZ.

The Rosenthal solution provides guidance and helps us understand the role of welding speed and power input. Nevertheless, a number of very important aspects of the welding process are naturally omitted. The most obvious is that real weld beam would not be a point source. In many cases, the power can be well represented by a Gaussian distribution, whose total energy is equal to Q as above, and whose width depends on processing variables, such as beam shape, plasma flow, stand-off distance,

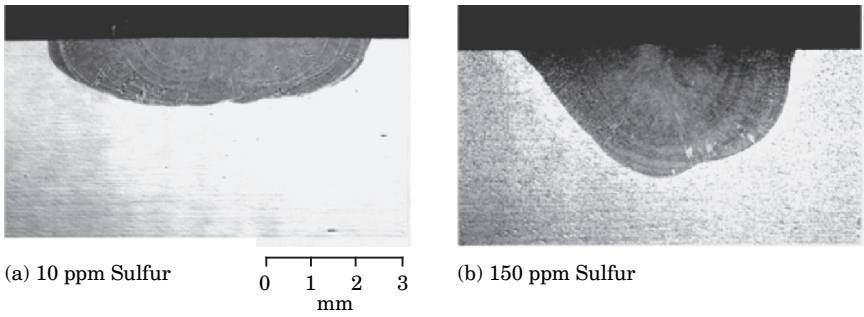

Fig. 1.12 Cross-sections of type 304 stainless steels after GTA welding. (a) 10 ppm sulfur content. (b) 150 ppm sulfur content. Reproduced with permission from Pierce, et al. [11].

etc., relative to the particular type of welding. Far away from the source, however, the Rosenthal solution might still provide a reasonable estimate.

Another very important phenomenon that is not included is the effect of fluid flow within the weld pool. The flow may be driven by electromagnetic effects in arc welding, but perhaps a more interesting source is flow driven by gradients in surface tension on the weld pool surface, a phenomenon sometimes referred to as the *Marangoni effect*. Because of the strongly concentrated energy source, a large temperature gradient is often induced on the surface.[1] If the surface tension $\gamma_{\ell a}$ depends on temperature, then the temperature gradient induces a surface flow that can have a considerable influence on the melting pattern. If the surface tension increases with temperature ($d\gamma_{\ell a}/dT > 0$), the liquid moves toward the weld beam on the surface, inducing a narrower and deeper pool. On the other hand, if the surface tension decreases with temperature ($d\gamma_{\ell a}/dT < 0$), the surface flow moves away from the weld beam, leading to a wider and shallower pool. This phenomenon is very important in the welding of steels, where the sign of $d\gamma_{\ell a}/dT$ is actually reversed as the sulfur content in the steel increases. Low-sulfur steels are often specified for welding to avoid cracking problems associated with MnS "stringers" in the HAZ. However, $d\gamma_{\ell a}/dT < 0$ for these compositions, which renders it difficult to ensure sufficient penetration for welding of thick plates. Welders thus sometimes add sulfur to the weld shielding gas to increase the concentration in the weld pool enough for $d\gamma_{\ell a}/dT > 0$, thereby allowing deep penetration welds to be made.

This phenomenon is illustrated in Fig. 1.12, which shows cross-sections of gas-tungsten arc (GTA) welds made on type 304 stainless steel [11]. The melted region is clearly delineated by etching. When the

[1] In the Rosenthal solution, where there is a point source, the temperature gradient at the weld beam is infinite. This is clearly not the case in reality, but it nevertheless indicates that the temperature gradient can be very large.

sulfur content is low (10 ppm, Fig. 1.12a), the weld pool is relatively shallow, because at this sulfur content, $d\gamma_{\ell a}/dT < 0$, leading to a surface flow on the weld pool away from the beam. At higher sulfur content (150 ppm, Fig. 1.12b), the sign of $d\gamma_{\ell a}/dT$ reverses, and the surface flow is directed toward the weld beam, leading to a deeper penetration weld.

1.3 Summary

This chapter provides an overview of the content and coverage of this book. In the three parts that follow, we first describe the fundamental aspects of thermodynamics, phase diagrams and analytical techniques that are employed in the subsequent parts. These concepts are then used in Part II to describe the evolution of microstructures, beginning with nucleation, continuing with dendritic growth and structures in eutectic and peritectic alloys, and concluding with a chapter on microsegregation. The final part combines the fundamentals from Part I with the understanding of microstructure to examine defects that may appear during solidification. This chapter also describes several important solidification processes, focusing on those aspects that motivate the further studies addressed in the remainder of the text.

References

[1] *ASM Handbook - Volume 6, Welding*. ASM International, Metals Park, OH, 1993.
[2] *ASM Handbook - Volume 15, Casting*. ASM International, Metals Park, OH, 2008.
[3] North american die casting association. URL, 2008. http://diecasting.org/castings.
[4] Sand casting. Wikipedia, 2008. http://en.wikipedia.org/wiki/Sand_casting.
[5] J. Campbell. *Castings: The new metallurgy of cast metals*. Butterworth-Heinemann, 2003.
[6] B. Cantor and K. O'Reilly, editors. *Solidification and casting: an Oxford-Kobe materials text*. CRC Press, 2003.
[7] B. Chalmers. *Principles of solidification*. Wiley, New York, 1964.
[8] M. C. Flemings. *Solidification Processing*. McGraw-Hill, New York, 1974.
[9] R. W. Heine, C. R. Loper, and P. C. Rosenthal. *Principles of metal casting*. McGraw-Hill, New York, 1967.
[10] W. Kurz and D. J. Fisher. *Fundamentals of Solidification*. Trans. Tech. Publ., Aedermansdorf, Switzerland, 4th edition, 1998.
[11] S. W. Pierce, P. Burgardt, and D. L. Olson. Thermocapillary and arc phenmoena in stainless steel welding. *Welding journal*, 78:45S – 52S, 1999.
[12] D. M. Stefanescu. *Science and engineering of casting solidification*. Kluwer Academic/Plenum, New York, 2nd edition, 2002.
[13] R. Trivedi. *Materials in art and technology*. Taylor Knowlton, 1998.
[14] K-O Yu. *Modeling for casting and solidification processing*. CRC Press, 2001.

Part I

Fundamentals and Macroscale Phenomena

This part of the book treats the most classical aspects of solidification, i.e., those that can be viewed at the macroscopic scale. It also introduces several fundamental concepts that form the foundation for study. In Chap. 2, the thermodynamics of solidification processes is considered, introducing the important concepts of free energy, chemical potential and equilibrium. We also discuss departure from equilibrium induced by capillarity and kinetics. These concepts, which are then applied throughout the book, are generalized and put into a compact form in Chap. 3, where we describe equilibrium phase diagrams for binary and ternary systems. However, thermodynamics tells only what *should* happen, i.e., it identifies the state of the system that has the lowest energy at equilibrium. It does not guarantee that this *will* happen, nor does it include any information about how the system evolves from one state to another in time. For this, we need to include transport phenomena and departures from equilibrium associated with curved surfaces and moving interfaces.

Chapter 4 presents the balance equations for mass, momentum, energy and solute transport. We also introduce the constitutive models for heat and solute transport most often used to devise a complete set of governing equations. These conservation equations are integrated over a representative volume element of the microstructure in order to obtain two sets of equations: average equations applicable at the macroscopic scale, and interfacial balances at moving interfaces that can be used at the microstructure level. Finally, this chapter introduces the concepts and methods for scaling the governing equations to identify the important (and negligible) terms. The scaling process is essential for the study of solidification microstructures because it allows for the separation of time and length scales for heat and solute transport. These are the basic concepts behind microstructure pattern formation, mediated by surface tension forces.

In Chap. 5, several fundamental solidification problems having analytical solutions are presented. Some of the most important dynamic features of solidification are identified in these problems: the separation of length scales for heat and solute transport; the role of surface tension; the rate of growth of solidified layers in molds; and the curious inability of transport alone to predict growth patterns. These features become the basis for studying microstructure formation in Part II.

Finally, Chap. 6 describes some of the important aspects of numerical methods for analyzing solidification. First, fixed grid methods based on average balance equations are presented in order to describe solidification processes at the macroscopic scale. Then, we describe front tracking methods that follow the moving phase boundary on a discrete grid. Some of the problems presented in Chap. 5 are used as test cases for the numerical schemes in order to illustrate the techniques used to attack the moving boundary problem.

CHAPTER 2

THERMODYNAMICS

2.1 Introduction

Thermodynamics is the study of the behavior of systems of matter under the action of external fields such as temperature and pressure. It is used in particular to describe equilibrium states, as well as transitions from one equilibrium state to another. In this chapter, we introduce the concepts pertinent to solidification. It is assumed that the reader has had some exposure to classical thermodynamics; thus, the presentation is more in the form of definitions and reviews than what might be found in a standard thermodynamics text. We begin with a brief review of basic concepts, and then proceed to develop the relationships needed in future chapters, with a focus on condensed phases, i.e., liquids and solids.

The *system* consists of all of the matter that can interact within a space of defined boundary. A system may contain several *components*, chemically distinct entities such as elements or molecules. There may also be several *phases*, which are defined as portions of a system that are physically distinct in terms of their state (solid, liquid, vapor), crystal structure or composition. For example, pure water is considered as a single component, H_2O, that may exist as several different phases, such as ice, liquid or steam. In binary alloys, such as mixtures of Al and Cu, various phases can be present, including a liquid in which both elements are completely miscible; limited solid solutions of Cu in Al and Al in Cu; and intermetallic compounds such as Al_2Cu, etc.

For a single component, or *unary* system, there are three thermodynamic variables: the temperature T, the pressure p and the volume V. These variables define the state of the system. However, only two are independent, and the third is obtained through an *equation of state*, e.g., $V = V(p, T)$. The ideal gas law is one of the most familiar equations of state, but such an equation of state exists for all materials. Note that T and p are *intensive* variables, meaning that they do not depend on the amount of material present, whereas V is an *extensive* variable, which means that its value does depend on the quantity of material present in the system. A *state variable* is one which can be written as a function

of the thermodynamic variables. For example, the *internal energy* of the system E is a state variable which is also extensive. We will use upper case characters to designate extensive state variables such as E, G, H, S, V (these symbols will be defined as they appear below). An intensive form of any extensive state variable can be formed by dividing it by the total mass M, or by the total number of moles n in the system. The former is called the *specific* form and is represented by the corresponding lower case character, e, g, h, s, v. The latter is called the *molar* form, denoted by the superscript m, i.e., E^m, G^m, H^m, S^m, V^m. For example, the specific internal energy of the system is $e(T, V) = E/M$, whereas the molar internal energy is given by $E^m(T, V) = E/n$.

In the following sections, we first introduce the concepts of classical thermodynamics for systems having one component (unary systems), then we treat the case of binary alloys, introducing the entropy and enthalpy of mixing as well as ideal and regular solutions. In particular, the regular solution model, despite its relative simplicity, is able to produce a rich variety of solidification reactions, e.g., eutectics, peritectics or monotectics, and solid state transformations (e.g., spinodal decomposition, ordering, etc.). This makes the model a very useful tool for describing the relationship between the molar Gibbs free energy and phase transformations. Differentiation of the free energy leads to the *chemical potential*, which is an indispensable concept for understanding phase transformations.

The subject then turns to the thermodynamics of multi-component systems. It will be seen that, as the composition space is enriched by adding more components, more phases can co-exist. The treatment above is then generalized to define the conditions of equilibrium for a multi-component, multi-phase system. This takes the form of *Gibbs' phase rule*, which gives the number of degrees of freedom of a multi-component system as a function of the number of co-existing phases. The concepts developed in this chapter are later used and enlarged in Chap. 3, which is devoted to equilibrium phase diagrams for binary and ternary systems.

Finally, we discuss the phenomena that lead to modification or departure from equilibrium. The effect of surface energy and curvature on thermodynamic equilibrium is first derived for a static interface. This is extremely important for the understanding of microstructure development in later chapters. We also introduce the concept of disequilibrium at a moving solid-liquid interface due to kinetic effects; this effect is related to the ability of atoms and species in the liquid to rearrange themselves into a crystalline phase.

2.2 Thermodynamics of unary systems

2.2.1 Single phase systems

In thermodynamics, one compares different states and the corresponding relative changes in the various thermodynamic quantities. Often, the

states being compared are "close" to each other, meaning that the kinds of change under scrutiny are incrementally small. Consider the internal energy of the system E, which is a state variable for a whole system of volume V. The difference dE between two states is an exact differential. Choosing T and V as the independent state variables, we may write the following:

$$dE(T,V) = \left(\frac{\partial E}{\partial T}\right)_V dT + \left(\frac{\partial E}{\partial V}\right)_T dV \tag{2.1}$$

One changes variables frequently in this subject, so it is necessary to designate which variables are held constant by use of the subscript on the parenthesis. The partial derivatives that arise from such forms are often given special names and symbols. For example, $(\partial e/\partial T)_V = c_V$ is called the specific heat at constant volume (units $\mathrm{J\,kg^{-1}\,K^{-1}}$).

We shall see that T and V are not the natural variables to express the energy for condensed phases. The change in internal energy in the system is the sum of any heat added to the system, designated δQ, plus work done by external forces, designated δW. The *First Law of Thermodynamics* is a translation of this statement into the equation

$$dE = \delta Q + \delta W \tag{2.2}$$

For a gas or a liquid, the work arises only by compression, and thus $\delta W = -pdV$. However, for a solid, there may be other contributions from the other components of the stress tensor, as will be seen in Chap. 4. Electromagnetic contributions can also enter into δW. The variations δQ and δW are written with the symbol δ to indicate that their value is path-dependent, and thus both Q and W are not state variables. In this chapter, we consider only the hydrostatic compression/expansion term, $\delta W = -pdV$.

It is useful to separate δQ into a *reversible* part δQ_{rev} and an *irreversible* part δQ_{irr}. When following a reversible path, i.e, a succession of infinitesimally close equilibrium states, $\delta Q_{irr} = 0$. This concept of irreversibility leads to definition of the *entropy* $S(T,V)$, a state variable, defined such that for a reversible path one has

$$dS = \frac{\delta Q_{rev}}{T} \tag{2.3}$$

Notice that even though δQ_{rev} is not a state variable, the entropy is. The *Second Law of Thermodynamics* is the statement that, for any process, $\delta Q_{irr} \geq 0$. We will be concerned almost entirely with equilibrium processes, where $\delta Q_{irr} = 0$. This also implies that at equilibrium, the system has attained its minimum energy and maximum entropy. The first law, Eq. (2.2), can now be written in terms of the entropy

$$dE = \delta Q - pdV = TdS - pdV \tag{2.4}$$

In this form, the internal energy seems to be naturally expressed in terms of the two extensive variables, S and V. Unfortunately, this form

is not very convenient for condensed phases. For example, how would you measure the specific heat at constant volume, c_V, i.e., the increment of internal energy of the system while keeping its volume constant? You would of course use a calorimeter. But constraining the volume to remain constant during the test would be very difficult. Therefore, one defines another state variable, the enthalpy H:

$$H = E + pV \tag{2.5}$$

The enthalpy will be used extensively in the analysis of solidification. Using Eq. (2.4), the differential of H is given by

$$dH = dE + pdV + Vdp = TdS + Vdp \tag{2.6}$$

Considering $H = H(S, p)$, we have

$$dH = \left(\frac{\partial H}{\partial S}\right)_p dS + \left(\frac{\partial H}{\partial p}\right)_S dp \tag{2.7}$$

By comparison with Eq. (2.6) we may identify

$$\left(\frac{\partial H}{\partial S}\right)_p = T; \quad \left(\frac{\partial H}{\partial p}\right)_S = V \tag{2.8}$$

Dividing by the constant mass of the system, M, and using Eq. (2.8) gives

$$dh = Tds + vdp \tag{2.9}$$

At constant pressure, the second term vanishes, and thus only the heat brought to the system contributes to dh. For this reason, the enthalpy is also sometimes called the *heat content*. By writing $h = h(T, p)$, and applying the chain rule for differentiation, we can define c_p, the *specific heat at constant pressure* as:

$$c_p = (\partial h/\partial T)_p \tag{2.10}$$

Thus, at constant pressure $dh = c_p dT$. It follows from Eq. (2.10) that c_p can be measured in an adiabatic calorimeter maintained at constant pressure, rather than at constant volume, which is certainly much more convenient!

In practice, the enthalpy is computed by integrating measured values of c_p over temperature, with the constant of integration adjusted in such a way that the enthalpy is zero at 298 K:

$$h(T) = \int_{298\ \mathrm{K}}^{T} c_p(\theta) d\theta \tag{2.11}$$

It also follows from Eq. (2.9) that the specific entropy, $s(T)$, is given at constant pressure by

$$ds = \left(\frac{dh}{T}\right)_p = \frac{c_p dT}{T} \Rightarrow s(T) = \int_{0\ K}^{T} \frac{c_p(\theta)}{\theta} d\theta \tag{2.12}$$

Note that the convention is to choose the reference temperature for the entropy to be 0 K, rather than ambient temperature, so that the entropy is zero at absolute zero. It is left as an exercise to show that

$$c_p - c_V = \left(\left(\frac{\partial e}{\partial v} \right)_T + p \right) \left(\frac{\partial v}{\partial T} \right)_p \tag{2.13}$$

Perhaps the most important thermodynamic state variable for solidification is the *Gibbs free energy*, G, which is used extensively throughout this book. It is defined as

$$G = H - TS \tag{2.14}$$

Computing the differential dG and using Eq. (2.6), we obtain

$$dG = dH - SdT - TdS = Vdp - SdT \tag{2.15}$$

from which we see that the Gibbs free energy is naturally expressed in terms of the two intensive variables, p and T. In other words, if the pressure and the temperature are known for a unary system, its Gibbs free energy per unit mass or per mole is unambiguously specified. From Eq. (2.15), one sees that

$$S = -\left(\frac{\partial G}{\partial T} \right)_p ; \qquad V = \left(\frac{\partial G}{\partial p} \right)_T \tag{2.16}$$

Figure 2.1 shows schematically the variation of the enthalpy of a single phase with temperature. Note that the value of c_p may be approximately constant at room temperature (i.e., linear $h(T)$), but as $T \to 0$ K, the specific heat must tend towards zero faster than the temperature. Figure 2.1 also shows the specific Gibbs free energy.

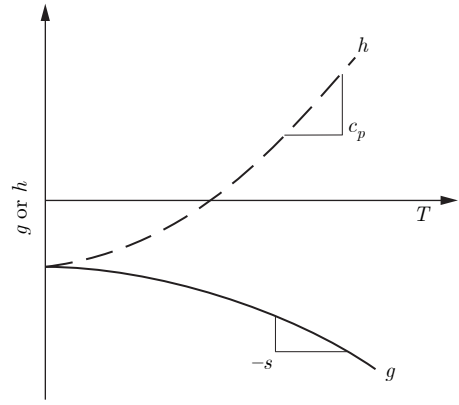

Fig. 2.1 Free energy and enthalpy as a function of temperature.

2.2.2 Equilibrium of phases

The second law of thermodynamics stated that the free energy of a closed system at equilibrium must be minimum (or its entropy maximum). For a system consisting of a single, homogeneous phase, Eq. (2.15) implies that both the temperature and pressure are uniform.

Consider now a closed system consisting of two phases α and β (e.g., solid and liquid, liquid and vapor, two crystalline phases, etc.). Assume that mechanical and thermal equilibrium have been established, i.e., that the temperature and pressure are fixed. The Gibbs free energy of the system can be written as the following sum:

$$G = n_\alpha G^m_\alpha + n_\beta G^m_\beta \tag{2.17}$$

where G^m_α and G^m_β are the molar Gibbs free energies of the two phases, and n_α and n_β are the number of moles of each phase. Since the system is closed, the constraint $(n_\alpha + n_\beta) = n = \text{constant}$ must be satisfied. It is convenient to choose one mole for the whole system, in which case one has $G^m = \chi_\alpha G^m_\alpha + \chi_\beta G^m_\beta$, where we have introduced the mole fractions of the phases χ_i, which have the property $\chi_\alpha + \chi_\beta = 1$. Since equilibrium corresponds to a minimum energy, matter must be repartitioned between the two phases until at equilibrium we have

$$\frac{\partial G^m}{\partial \chi_\alpha} = 0 = G^m_\alpha - G^m_\beta \tag{2.18}$$

We obtain the important property that at equilibrium, a unary system consisting of two phases must satisfy the following conditions:

- $T_\alpha = T_\beta = T$ (thermal equilibrium)
- $p_\alpha = p_\beta = p$ (mechanical equilibrium)
- $G^m_\alpha = G^m_\beta = G^m$ (phase equilibrium)

These relations can be thought of as constraints on the system. Gibbs defined the *degrees of freedom* of a system, designated N_F, as the number of independent variables (T, p and, as we will see later, composition) which can be changed and still maintain the same number of phases in equilibrium. When two phases are present, their pressure and temperature must be equal, so from four potential variables $(T_\alpha, T_\beta, p_\alpha, p_\beta)$ the number of independent variables is reduced to two (T and p) by the constraint of equilibrium. The equality of the Gibbs free energies of the two phases further reduces the number of degrees of freedom by one, e.g., fixing the pressure implies that the temperature is also given. This is familiar for water: at atmospheric pressure at sea level, ice melts at $0°$C (co-existence of ice and water) and water boils at $100°$C (co-existence of water and vapor).

Figure 2.2 shows schematically the variation with temperature of the molar enthalpy and Gibbs free energy of the solid and liquid phases of a

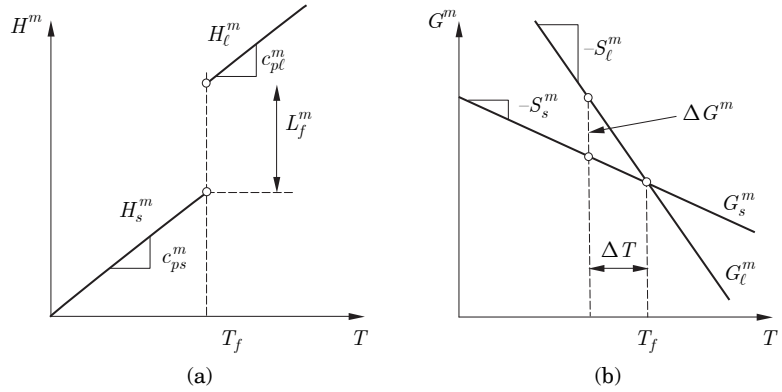

Fig. 2.2 Molar enthalpy (a) and molar Gibbs free energy (b) for the liquid and solid phases of a pure substance as a function of temperature.

pure substance at atmospheric pressure. The point where the free energies of the two phases are equal defines the equilibrium melting point T_f. Note that the slope of G_ℓ^m is greater (in absolute value) than that of G_s^m, since the liquid is more disordered than the solid. The difference in slopes, i.e., $\Delta S_f^m = S_\ell^m - S_s^m$, is called the *entropy of fusion*, and it may be computed using the fact that the molar Gibbs free energy of the liquid and solid phases are equal at T_f.

$$\begin{aligned} G_\ell^m(T_f) - G_s^m(T_f) = 0 &= [H_\ell^m(T_f) - T_f S_\ell^m(T_f)] - [H_s^m(T_f) - T_f S_s^m(T_f)] \\ &= [H_\ell^m(T_f) - H_s^m(T_f)] - T_f\,[S_\ell^m(T_f) - S_s^m(T_f)] \\ 0 &= L_f^m - T_f \Delta S_f^m \\ \text{or}\quad \Delta S_f^m &= \frac{L_f^m}{T_f} \end{aligned} \tag{2.19}$$

where L_f^m is the molar enthalpy of fusion, more often called the *latent heat of fusion* per mole. It corresponds to the increase of enthalpy in the liquid phase at the melting point, as illustrated in Fig. 2.2. It will be useful in later chapters to consider the free energy change upon solidification at some temperature T below the melting temperature $T = T_f - \Delta T$, where ΔT is called the *undercooling* (see Fig. 2.2). The Gibbs free energy change upon melting at temperature T is

$$G_\ell^m(T) - G_s^m(T) = -\Delta G^m(T) = (H_\ell^m(T) - H_s^m(T)) - T(S_\ell^m(T) - S_s^m(T)) \tag{2.20}$$

If the undercooling is small, then it can be shown (see Exercise 2.5) that the enthalpy change at temperature T, $(H_\ell^m(T) - H_s^m(T))$ is the same as at temperature T_f, i.e., $L_f(T) = L_f(T_f)$, and similarly that $\Delta S_f^m(T) = \Delta S_f^m(T_f)$. Substituting these relations into Eq. (2.20) and using Eq. (2.19) yields the result:

$$\Delta G^m(T) = -\Delta S_f^m \Delta T \tag{2.21}$$

What happens to the equilibrium melting point if the pressure changes by an incremental amount dp? The incremental variation in G^m for each phase must be the same for equilibrium to be re-established. Applying Eq. (2.15) in molar form to each phase, we have

$$dG_\ell^m = V_\ell^m dp - S_\ell^m dT \tag{2.22}$$
$$dG_s^m = V_s^m dp - S_s^m dT \tag{2.23}$$

Setting $dG_\ell^m = dG_s^m$ and subtracting Eq. (2.23) from Eq. (2.22) gives the *Clausius-Clapeyron* equation

$$\left.\frac{dp}{dT}\right|_{s\ell} = \frac{\Delta S_f^m}{\Delta V_f^m} = \frac{L_f^m}{T_f \Delta V_f^m} \tag{2.24}$$

where ΔV_f^m is the molar volume change upon melting. For most materials, $\Delta V_f^m > 0$. Water and bismuth are two rare exceptions. The subscript $s\ell$ indicates that the slope corresponds to the solid-liquid phase boundary. One can derive a similar expression for the vaporization reaction, replacing the volumes, enthalpies and entropies by the appropriate values.

When three phases are present (e.g., solid, liquid and vapor), one obtains, by similar arguments, the result that equilibrium is defined by: $T_\alpha = T_\beta = T_\gamma = T; p_\alpha = p_\beta = p_\gamma = p; G_\alpha^m = G_\beta^m = G_\gamma^m = G^m$. This imposes another constraint on the system, reducing N_F to zero. Such points in phase diagrams, where $N_F = 0$, are called *invariant points*. This means that the three phases can coexist only at a unique pressure and temperature (called the *triple point* in this case).

The information we have just described can be summarized in an equilibrium phase diagram, which shows the phases present at various values of T and p. Figure 2.3 shows an example for water. The solid curves are phase boundaries, also called curves of two-phase coexistence. The intersections of two-phase coexistence curves where all three phases coexist are called triple points. Notice that there are two such points in the diagram, one for water, vapor and Ice I at 0.01°C and 612 Pa, and a second involving water, Ice I and Ice III at about -20°C and about 5×10^8 Pa. The slope of the two-phase coexistence curves is given by the Clausius-Clapeyron equation, Eq. (2.24). Water is an unusual material in that its molar volume decreases upon melting, which results in a liquid-solid coexistence curve of slightly negative slope. For most materials, the slope is positive, like the liquid-vapor and solid-vapor curves.

Let us conduct some "thought" experiments at atmospheric pressure p_a, as indicated in Fig. 2.3. Beginning at high temperature, where $T > T_v(p_a)$, only the vapor phase exists. Now, the system is cooled with a fixed heat extraction rate per unit mass, $\dot{h} < 0$. The cooling rate $\dot{T}$ of the vapor phase is given by $\dot{h}/c_{pg}$, as indicated in Fig. 2.4. As the temperature decreases, the liquid-vapor phase boundary is encountered at temperature T_v, commonly called the boiling point. The two phases coexist at T_v until all of the vapor has transformed to liquid. Note the very large isothermal

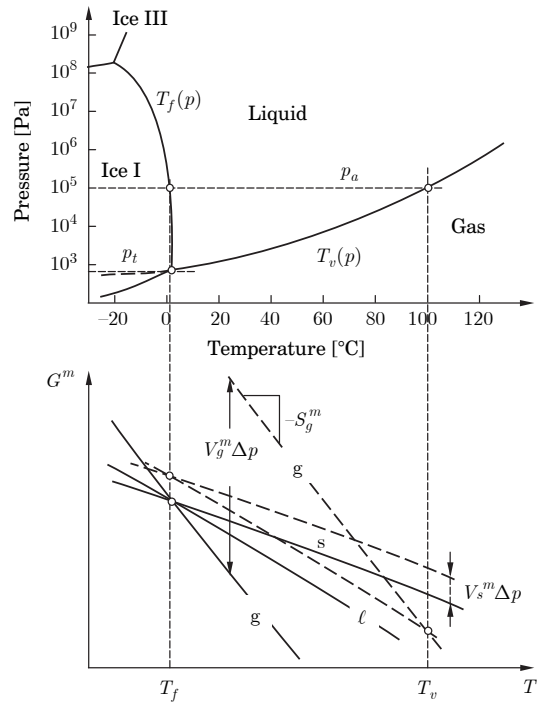

Fig. 2.3 Equilibrium phase diagram for water and schematic Gibbs free energies of the solid, liquid and gas phases at atmospheric pressure p_a (dashed curves) and at the triple point pressure p_t (solid lines). This figure is only schematic as $V_g^m \approx 1250\, V_\ell^m$.

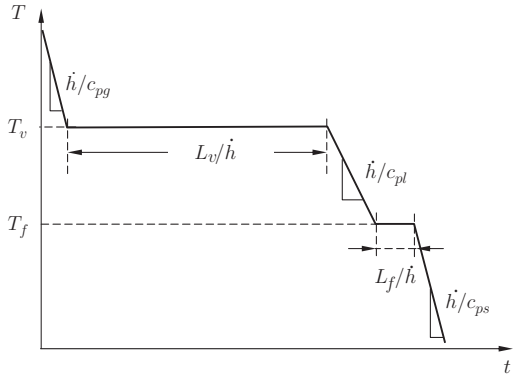

Fig. 2.4 Thermal history of a water sample cooled with a constant heat extraction rate, $\dot{h} < 0$, at atmospheric pressure. As $c_{p\ell} \approx 2c_{pg} \approx 2c_{ps} = 4.18\ \mathrm{J\,g^{-1}\,K^{-1}}$, note that the cooling rate of the liquid is half that of the two other phases. Also, since $L_v = 2250\ \mathrm{J\,g^{-1}}$ and $L_f = 333\ \mathrm{J\,g^{-1}}$, the time for condensation is much longer than the time for solidification.

plateau associated with condensation of water: it is a direct measure of the very large enthalpy of vaporization (or condensation). If the cooling curve had instead continued with the same slope, this would correspond to a temperature at the end of the plateau more than 1000°C below T_v. After all the vapor has condensed, the temperature can once again decrease. Because the specific heat of water is about twice that of the vapor, the cooling rate ($\dot{T}$) is about half of the value before condensation if we maintain a constant rate of heat extraction $\dot{h}$. When reaching the melting point T_f, the temperature again remains at the plateau until all of the liquid has solidified. Notice the difference in the duration of the arrest at T_f compared to the arrest at T_v, reflecting the difference in magnitude of the latent heats of fusion and vaporization.

Suppose that we were to repeat the preceding thought experiment at slightly lower pressure, e.g., on the top of Mount Everest where the pressure is only about $0.3\,p_a$. What would change? We would traverse the phase diagram along an isobar parallel to p_a at $p = 30$ kPa. The results would be qualitatively similar, but the values we would observe for T_f and T_v would change. Note, however, that because the slopes of the lines of two-phase separation are different, the change in boiling point would be much larger than the change in melting point (water boils at around 70°C at the top of Mount Everest). It also should be pointed out that the experiment of boiling water when performed in a kitchen is different from the one proposed here: indeed, the kitchen's atmosphere is not a unary system as we have a mixture of vapor and air, itself made of many species (nitrogen, oxygen, carbon dioxide, etc.). On the other hand, if water vapor is initially the only species in a closed vessel, the equation of state for the vapor phase ($pV = nRT$ if it is assumed to be ideal), imposes that the pressure cannot remain constant upon cooling and later during condensation (see Exercise 2.2).

Figure 2.3 also includes Gibbs free energy curves for the three phases at atmospheric pressure p_a (dashed lines) and at the triple-point pressure, $p_t = 612$ Pa (solid lines). Note that these curves are only schematic, as the molar volume of the vapor phase is about 1250 times that of the condensed phases. Free energy is a very powerful tool for understanding the relationships between the phases. At p_t, the three curves intersect at the triple point (0.01°C), where the free energies of all three phases are equal. Recall from Eq. (2.16) that

$$S^m = -\left(\frac{\partial G^m}{\partial T}\right)_p ; \qquad V^m = \left(\frac{\partial G^m}{\partial p}\right)_T \tag{2.25}$$

Thus, the slope of each curve is negative, and the magnitudes of the slopes, i.e., the entropy of the phases, are in the order $S^m_s < S^m_\ell < S^m_g$. When the pressure is increased to p_a, each curve shifts upward, resulting in a new curve approximately parallel to the original. The magnitude of the shift is proportional to its specific volume (note that the specific volume will also vary between p_t and p_a). Because the specific volume of liquid water is

smaller than that of the solid near the melting point, the liquid free energy curve shifts slightly less than the corresponding curve for the solid. This decreases the solid-liquid equilibrium from $T_t = 0.01°\text{C}$ to $T_f = 0°\text{C}$. By the same reasoning, we see that the free energy curve for the gas shifts more than those of the other two phases. The intersection points of the phase curves are projected back to the phase diagram, as shown. Fig. 2.3 also shows (as a heavy dashed line) the continuation of the liquid-gas two phase equilibrium curve past the triple point, extending into the "Ice I" region. If the solid Ice I were to somehow fail to appear, then the system would remain liquid, i.e., it would follow this projection for this range of temperatures and pressures. This is called *metastable equilibrium*, because there is a different transformation between solid and gas that has lower energy. The concept of metastable extensions to the lines in the phase diagrams will prove to be very useful in later chapters for understanding microstructure development.

2.3 Binary alloys

2.3.1 Thermodynamics of a single phase solution

We now extend the treatment developed in the previous section to the thermodynamics of binary mixtures. For the moment, the mixture will be assumed to consist of a single phase, i.e., a *solution* of the two components. Consider the volume illustrated in Fig. 2.5, composed of a homogeneous phase made up of two components, labeled A and B. The components A and B may be atoms or molecules. B is assumed to be the minor component and is called the *solute*, whereas the major component A is the *solvent*. In addition to the thermodynamic variables introduced in the previous section, we now need additional variables to completely specify the state of the system; specifically we need to describe the *composition*. The system contains n_A moles of component A, and n_B moles of species B. The total

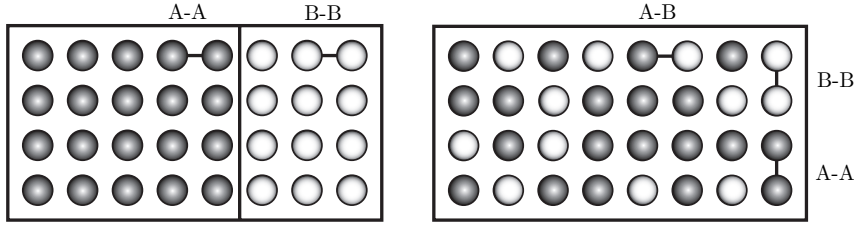

(a) Before mixing (b) After mixing

Fig. 2.5 Schematic of the mixing of n_A moles of A atoms/molecules with n_B moles of B atoms/molecules. Before the components are mixed, there are only A-A and B-B bonds; upon forming a solution, some of these bonds are replaced by A-B bonds. This becomes important when we discuss the free energy of the solution.

number of moles $n = n_A + n_B$. We can also specify the composition using the mole fractions of each component, X_A and X_B, defined as

$$X_A = \frac{n_A}{n_A + n_B}; \qquad X_B = \frac{n_B}{n_A + n_B} \tag{2.26}$$

Other possible representations of the composition are discussed in Chap. 3. By their definitions, it follows that $X_A + X_B = 1$. One can choose to use the n_J or the X_J to represent the composition, as long as the constraints on the X_J are kept in mind.

Because the molecules or atoms interact when they are mixed, the Gibbs free energy of the solution varies with composition, as well as with temperature and pressure. Writing $G = G(T, p, n_A, n_B)$, the differential dG becomes

$$\begin{aligned} dG(p, T, n_A, n_B) = V(p, T, n_A, n_B)dp - S(p, T, n_A, n_B)dT \\ + \mu_A(p, T, X_B)dn_A + \mu_B(p, T, X_B)dn_B \end{aligned} \tag{2.27}$$

where we have introduced the *chemical potential* of each species, μ_A and μ_B, defined as

$$\mu_A = \left(\frac{\partial G}{\partial n_A}\right)_{p,T,n_B}; \qquad \mu_B = \left(\frac{\partial G}{\partial n_B}\right)_{p,T,n_A} \tag{2.28}$$

Note that the chemical potentials are intensive variables, which is why in Eq. (2.27) they are not written as functions of n_A and n_B, but rather as functions of the mole fraction X_B. We could have chosen X_A instead of X_B, since we know that $X_A + X_B = 1$. Dividing Eq. (2.27) by n allows us to write the expression in terms of molar quantities:

$$\begin{aligned} dG^m(p, T, X_B) = V^m(p, T, X_B)dp - S^m(p, T, X_B)dT \\ + (\mu_B(p, T, X_B) - \mu_A(p, T, X_B))dX_B \end{aligned} \tag{2.29}$$

where we have invoked the relation $dX_A = -dX_B$.

One might then wonder how the molar Gibbs free energy of the system varies with composition at constant temperature and pressure. G is called a *homogeneous function* of the n_J, meaning that its magnitude is directly proportional to the amount of its constituents, so at constant temperature and pressure we have

$$G = n_A\mu_A + n_B\mu_B \quad (\text{Fixed } T, p) \tag{2.30}$$

This expression is shown graphically in Fig. 2.6. Computing the differential of Eq. (2.30) gives:

$$dG = n_A d\mu_A + n_B d\mu_B + \mu_A dn_A + \mu_B dn_B \tag{2.31}$$

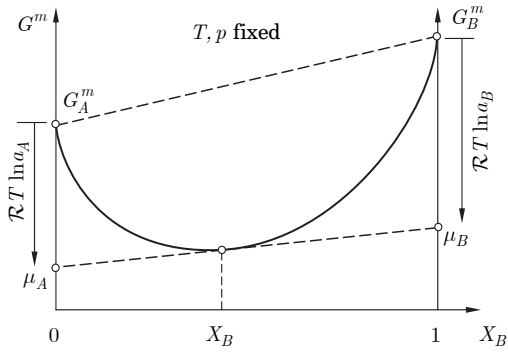

Fig. 2.6 Molar free energy of a binary solution as a function of the mole fraction of element B, showing the tangent construction to compute the chemical potentials μ_A and μ_B.

Taking T and p constant in Eq. (2.27), and equating dG with Eq. (2.31) yields the *Gibbs-Duhem* equation:

$$n_A d\mu_A + n_B d\mu_B = 0 \tag{2.32}$$

Dividing Eq. (2.32) by n, we obtain the following expression:

$$X_A d\mu_A + X_B d\mu_B = 0 \tag{2.33}$$

Next, we divide Eq. (2.30) by n, yielding

$$G^m = X_A \mu_A + X_B \mu_B \tag{2.34}$$

and then differentiate with respect to X_B:

$$\frac{\partial G^m}{\partial X_B} = \mu_B - \mu_A \tag{2.35}$$

Finally, combining Eqs. (2.34) and (2.35) yields the following two equations:

$$\begin{aligned} \mu_A(T, p, X_B) &= G^m(T, p, X_B) - X_B \left(\frac{\partial G^m}{\partial X_B} \right)_{T,p} \\ \mu_B(T, p, X_B) &= G^m(T, p, X_B) + (1 - X_B) \left(\frac{\partial G^m}{\partial X_B} \right)_{T,p} \end{aligned} \tag{2.36}$$

These equations define the *tangent rule construction* giving the chemical potential of components A and B for a solution having a composition X_B (see Fig. 2.6). The molar free energy G^m at that composition (and pressure and temperature) being known, the tangent to G^m at that point intersects the vertical axes, $X_A = 1$ and $X_B = 1$, at the values μ_A and μ_B, respectively.